

DESIGN OF CAPACITIVE WIRELESS POWER TRANSFER SYSTEMS WITH  
ENHANCED POWER DENSITY AND STRAY FIELD SHIELDING

by

Ujjwal Pratik

A thesis submitted in partial fulfillment  
of the requirements for the degree

of

MASTER OF SCIENCE

in

Electrical Engineering

Approved:

---

Zeljko Pantic, Ph.D.  
Major Professor

---

Regan Zane, Ph.D.  
Committee Member

---

Chris Winstead, Ph.D.  
Committee Member

---

Richard S. Inouye, Ph.D.  
Vice Provost for Graduate Studies

UTAH STATE UNIVERSITY  
Logan, Utah

2019

Copyright © Ujjwal Pratik 2019

All Rights Reserved

## ABSTRACT

Design of Capacitive Wireless Power Transfer Systems with Enhanced Power Density and  
Stray Field Shielding

by

Ujjwal Pratik, Master of Science

Utah State University, 2019

Major Professor: Zeljko Pantic, Ph.D.

Department: Electrical and Computer Engineering

Capacitive Power Transfer (CPT) appears as an alternative to proliferating Inductive Wireless Power Transfer technology (IPT). kW-range CPT systems with an EV vertical clearance of 10-15 cm have already been demonstrated. Among couplers used for CPT, Vertical 4-Plate Couplers (V4PCs) are preferred as being a compact solution, having rotational misalignment tolerance, and higher input-output self-capacitances. V4PCs have the capability to make CPT competitive with IPT. The mitigation of the leakage electric field safety hazard is one of the main challenges in CPT systems. Currently, there is no method developed for shielding of V4PC designs. Moreover, there is a lack of an analytical framework and fundamental models to better understand the relationship between the V4PC structure, compensation network topology, and the size of the active (unsafe) zone around the coupler.

In this thesis, the impact of the design of LC and LCL compensation networks on leakage electric field is presented. The results of this study can be used to minimize the area around a V4PC coupler where leakage electric field is above safety limits. FEM analysis and MATLAB circuit modelling are utilized to conduct this research. A comprehensive optimization algorithm is developed to find the optimum compensation to minimize the

active zone size. An experimental setup is built and experiments are conducted to verify optimization results.

(64 pages)

## PUBLIC ABSTRACT

Design of Capacitive Wireless Power Transfer Systems with Enhanced Power Density and  
Stray Field Shielding

Ujjwal Pratik

Wireless power transfer is becoming relevant today because of its effectiveness and convenience. It has been employed into consumer electronics such as cellular charging and electric vehicle charging. In general, inductive wireless power transfer (IPT) is mostly used for WPT. IPT requires coils and power transfer enhancing material such as ferrite to transfer power. However, Capacitive wireless Power Transfer (CPT) appears as an alternative because it requires cost effective and light metal plate couplers. Among CPT couplers, Vertical (stacked) Four-Plate Coupler (V4PC) structure offers the advantage of higher input and output self-capacitances, rotational misalignment.

Safety is one of the most important aspect of wireless power transfer. This thesis proposes a solution to minimize the leakage electric field of Vertical 4-Plate Couplers (V4PCs). It does so by finding the optimum value of circuit parameters. The effectiveness of the proposed solution is shown by experimental results.

This work is dedicated to my family and friends for their support.

## ACKNOWLEDGMENTS

I am thankful to my advisor Dr. Zeljko Pantic for his mentorship, constructive criticism and unconditional support. I am indebted to Dr. Pantic for allowing a novice to work under his guidance. Over the course of last two and half years, he has helped me become not only a better researcher but also a better person. Innumerable hours of intellectual discussion on wireless power transfer with Dr. Pantic have inspired me to continue my research after masters degree by pursuing PhD. Moreover, I would also like to express my sincere gratitude to my committee members Dr. Regan Zane, and Dr. Chris Winstead, for their guidance and encouragement.

This research would not have been possible without utilizing the excellent facilities at Utah State University Power Electronics Lab (UPEL) and Electric Vehicle and Roadway (EVR). I am grateful to the lab manager Ryan Bhom for his assistance. I am also thankful to UPEL colleagues, especially Reza Tavakoli, Chakridhar Reddy Teeneti, Ahmed Azad and Benny Varghese for their help and suggestions. I appreciate vibrant undergraduates Daniel Prieto, Jaydon Lord, and Johnathan Scheelke for their constant help and assistance. Finally, I would like to specially thank Tricia Brandenburg and Diane Buist for their assistance with administrative works.

Ujjwal Pratik

## CONTENTS

	Page
ABSTRACT .....	iii
PUBLIC ABSTRACT .....	v
ACKNOWLEDGMENTS .....	vii
LIST OF TABLES .....	x
LIST OF FIGURES .....	xi
1 INTRODUCTION .....	1
1.1 Background .....	1
2 LITERATURE REVIEW .....	4
2.1 CPT System .....	4
2.2 CPT Couplers .....	4
2.2.1 Single-wire CPT couplers .....	5
2.2.2 Lateral CPT couplers .....	5
2.2.3 Vertical (stacked) Four-Plate Coupler (V4PC) .....	6
2.3 Plate Capacitance Modelling .....	6
2.4 Safety Standards and Shielding Techniques .....	8
2.4.1 Safety Standards .....	8
2.4.2 Shielding Techniques .....	9
2.5 Compensation Network .....	10
3 STRAY FIELD CALCULATION AND MODELLING IN CAPACITIVE COUPLERS	
11	
3.1 Active Zone Around a Circular Two-Plate Coupler .....	11
3.2 Modelling The Active Zone .....	12
3.3 Active Zone Calculation .....	13
3.4 Active zone around a V4PC .....	16
4 OPTIMUM DESIGN OF COMPENSATION CIRCUIT FOR MINIMUM ACTIVE	
ZONE .....	19
4.1 Double-sided LC Compensation .....	19
4.2 Double-sided LCL Compensation .....	27
5 PRACTICAL CONSIDERATIONS OF AN V4PC IMPLEMENTATION .....	32
5.1 Design with Extended Outer Plates .....	32
5.2 Design with Shielding Plates .....	35
6 EFFICIENCY ANALYSIS OF FOUR PLATE CPT COUPLERS .....	38
6.1 Double-Sided LC compensation .....	39



7	EXPERIMENTAL RESULTS	41
7.1	Experimental Setup	41
7.2	Optimisation Results	43
7.2.1	Input Capacitance of Voltage Probe	46
7.2.2	Precision of LCR meter and Losses	47
8	CONCLUSION	48
	REFERENCES	49

## LIST OF TABLES

Table	Page
3.1 Coupler specifications and parameter values . . . . .	13
4.1 System specifications . . . . .	22
4.2 System specifications . . . . .	24
7.1 Experimental V4PC Specifications . . . . .	41
7.2 LCR meter measurements for capacitance calculation . . . . .	42
7.3 Circuit Parameters . . . . .	42

## LIST OF FIGURES

Figure	Page
2.1 Circuit model of a generalized CPT system. . . . .	4
2.2 CPT coupler types:(a) Single Wire, (b) Lateral Four-Plate, (c) Vertical Four-Plate (d) Vertical Four-Plate with circular plates (e) Vertical Four-Plate with chassis as P4 and the earth ground as P1. . . . .	5
2.3 Equivalent circuit models of a CPT coupler (a) inclusive model, (b) $\pi$ model, and (c) behavioral model. . . . .	7
2.4 Electric field guidelines for public exposure (ICNIRP 1998 and IEEE C95.1-2005). . . . .	8
2.5 Vertical six-plate coupler. . . . .	9
3.1 A contour diagram showing the magnitude of the electric field strength around a two-plate coupler. . . . .	11
3.2 Spheroid. . . . .	12
3.3 Test lines for electric field measurement. . . . .	14
3.4 Electric field calculated and simulated along the test lines (a) $TL_1$ and (b) $TL_2$ . . . . .	16
3.5 An electric field simulated for four-plate and two-plate couplers along the test lines (a) $TL_1$ and (b) $TL_2$ . . . . .	17
4.1 a) A CPT system with LC compensation networks and (b) its simplified functional model. . . . .	20
4.2 The Norton equivalent circuit of the transmitter side referred to the receiver. . . . .	20
4.3 The magnitude of $V_{14}$ for different compensation capacitance $C_{2,ext}$ and three different power ratings $P_{out}$ . . . . .	21
4.4 The impact of the capacitor selection on the $F_A$ and $F_V$ ( $V_{inv}=100$ V, $V_{out}=50$ V, and $P_{out}=300$ W). . . . .	22
4.5 Optimum compensation pairs $C_{1,ext,opt}$ and $C_{2,ext,opt}$ and optimum voltage $V_{14}$ as a function of $P_{out}$ . . . . .	23

4.6	Optimum compensation pairs $C_{1,ext,opt}$ and $C_{2,ext,opt}$ and optimum voltage $V_{14}$ as a function of $V_{inv}$ . . . . .	25
4.7	Optimum compensation pairs $C_{1,ext,opt}$ and $C_{2,ext,opt}$ and optimum voltage $V_{14}$ as a function of $V_{out}$ . . . . .	25
4.8	Comparison of optimum capacitances $C_{1,ext,opt}$ and $C_{2,ext,opt}$ for a symmetric coupler obtained by using eqn. (4.12) vs. (4.14). . . . .	26
4.9	The simplified functional model of an double-sided LCL compensated CPT. . . . .	27
4.10	The Norton equivalent circuit of the transmitter side referred to the receiver. . . . .	27
4.11	The magnitude of $V_{14}$ for different $C_{f2}$ and three different power ratings $P_{out}$ . . . . .	29
4.12	The impact of the capacitor selection on the $F_V$ and $F_A$ factors ( $P_{out}=300$ W). . . . .	29
4.13	Optimum $C_{f1,opt}$ and $C_{f2,opt}$ and optimum voltage $V_{14}$ as a function of $P_{out}$ . . . . .	30
5.1	A V4PC with a) extended outer plates, b) shielding plates P5 and P6. . . . .	33
5.2	The optimum values of $V_{14,opt}$ , radius $r_{E,opt}$ and height $h_{E,opt}$ of the active zone spheroid. . . . .	33
5.3	The ratio between the size of active zone for an arbitrary radius $r_o$ , and active zone for minimum $r_o=25$ cm ( $P_{out}=300$ W). . . . .	34
5.4	Distorted magnetic field contour at low voltage $V_{14}$ . . . . .	34
5.5	Impact of the inner plate size on $V_{14}$ , $V_{12}$ , and $V_{34}$ for LCL and LC compensations. . . . .	35
5.6	Impact of distance of shielding plates on $V_{56}$ for LCL compensation ( $r_{SH}=50$ cm, $P_{out}=300$ ). . . . .	35
5.7	Impact of distance of shielding plates on $F_V$ and $F_A$ . . . . .	36
5.8	Impact of size of shielding plates on $V_{56}$ ( $d_{SH}=8$ mm, $P_{out}=300$ W). . . . .	36
5.9	Impact of size of shielding plates on $F_V$ and $F_A$ . . . . .	37
6.1	Inclusive model of CPT coupler with losses. . . . .	38
6.2	Behavioral model with modeled eddy current losses in the plate. . . . .	38
7.1	Experimental Setup. . . . .	41
7.2	$V_{14}$ as a function of $C_{2,ext}$ . . . . .	43

7.3	Voltage ( $V_{inv}$ , $V_{14}$ ) and current ( $I_{L1}$ , $I_{Load}$ ) waveforms ( $C_{2,ext}=50.3$ pF) . .	43
7.4	$V_{43}$ and $V_{12}$ as functions of $C_{2,ext}$ . . . . .	44
7.5	$I_{C1,ext}$ and $I_{C2,ext}$ as a function of $C_{2,ext}$ . . . . .	44
7.6	$I_{L1}$ and $I_{L2}$ as a function of $C_{2,ext}$ . . . . .	45
7.7	Inductor ESR and plate losses as function of voltage $V_{14}$ . . . . .	45
7.8	Efficiency and output power as a function of $C_{2,ext}$ . . . . .	46

## CHAPTER 1

### INTRODUCTION

#### 1.1 Background

Over the past century, the transfer of electricity without wires has been one of the key challenge for researchers. Wireless Power Transfer (WPT) can provide convenience and safety over wired methods. Multiple methods of WPT have been developed, such as Inductive wireless Power Transfer (IPT), Capacitive wireless Power Transfer (CPT), energy harvesting. In general, IPT and CPT are used for short distances, while RF and Microwaves are used for long distances (upto thousand's of km's). These WPT techniques are active areas of research today.

WPT is applied across multiple domains. It is applied in consumer electronics (cell-phone charging) [1], transportation electrification (static and dynamic Electric Vehicles (EVs) charging) [2, 3], bio-medical implants (powering life-critical devices) [4], unmanned vehicle charging (underwater and aerial) [5, 6], space power transfer (sending power from Space to Earth) [7].

Currently, IPT is mostly favoured for short distance WPT because of low frequency requirement and high power density. IPT finds its application to wirelessly power EVs [1, 2, 8], consumer electronics [8–10], biomedical implants [11], autonomous aerial [12], or underwater vehicles [5, 13], etc. Historically, CPT was applied in low power applications to deliver power across an inherently small gap. The analysis conducted in [14] reports a superior coupler volumetric power density of CPT systems over the IPT systems for millimeter and submillimeter gaps between coupled plates, while the IPT dominates when the gap is greater than 1 mm. Nevertheless, CPT systems are demonstrated recently delivering kW's of power through a gap commensurable with the vertical clearance of EVs (10-20 cm), allowing CPT to be considered for charging of EVs, too. Nowadays, the list of CPT applications includes

charging of EVs, biomedical implants, and autonomous aerial vehicles [4, 15, 16], and many others.

One of the major advantages of CPT is that it allows power to be effectively transferred through an ungrounded metal barrier positioned between the transmitter and receiver [17]. Moreover, CPT does not require the use of ferromagnetic material (e.g. ferrites) to improve coupling or provide field shaping. Instead of expensive Litz wire, low cost metal plates (typically aluminum plates) are utilized to establish the field. This leads to comparatively lower system cost and less weight than in IPT couplers, and allows miniaturization of CPT couplers for small-gap applications [14]. In CPT systems, electric field lines are directed from a positive capacitor plate to a negative plate and they are comparatively better constrained in space than magnetic field lines of a coreless IPT coupler [18].

The main drawback of the CPT system is low coupling capacitance between plates (typically in pF range, except for very small gaps), which requires frequency in MHz range to reduce the reactance of coupling capacitors. Power of switching inverters operating in MHz range is still limited to low kW and sub-kW range, and boosting that power it is an active area of research.

Different structures of capacitive couplers are explored so far to provide a high-power, efficient, and compact CPT design. Brief analysis of different capacitive couplers is presented in Section 2.2. Vertical (stacked) Four-Plate Coupler (V4PC) structure has high rotational misalignment tolerance. Apart of a more compact and rigid structure, the V4PC, self capacitances dominantly created by metal plates on primary and secondary side can be used to replace or supplement critical capacitors in the primary and secondary compensation networks.

Safety is the major concern regarding WPT systems. The allowed levels of human exposure to electric and magnetic fields are limited by regulatory standards. In general, the leakage fields increase with increased power level for a given WPT system. V4PC has successfully been used to power EVs [19]. However there is a concern regarding the electric leakage field as demand for power level increases. There are two shielding approaches

proposed in literature to reduce or eliminate the leakage electric field in CPT systems: near-field phases-array cancellation technique and six plate capacitive couplers. There is no method developed for shielding of V4PC designs as both proposed methods are not applicable to V4PC designs.

Mitigating the electric leakage field for V4PC is a major research problem. This thesis proposes a solution to mitigate the electric leakage field for V4PC by focusing on compensation network design and geometrical modifications of V4PC structure. The thesis is an attempt to establish analytical and modeling fundamentals to better understand the relation between the V4PC structure, compensation network topology and design, and the size of active (unsafe) zone around the coupler. The active zone is defined as a region around the coupler where the electric field is greater than the human safety exposure limit. Various compensation networks are proposed in literature [3], and two commonly used networks (LC and LCL) will be analyzed in this article.

The objectives of this thesis are to: i) define quantitative measures of a successful shielding of CPT couplers, ii) define a methodology for calculating those parameters in a practical application, iii) determine the impact the design of LC and LCLC compensation networks has on the size of the active zone, iv) optimize the networks with the objective to minimize the size of safety zone, iv) explore the impact of practical aspects, such as chassis or earth ground on couplers shielding properties,v) explore the geometrical modifications of V4PC to reduce the size of an active zone.



## CHAPTER 2

### LITERATURE REVIEW

#### 2.1 CPT System

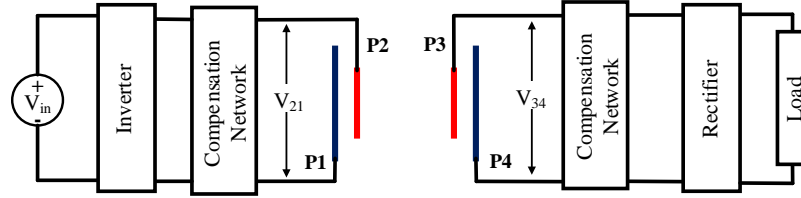


Fig. 2.1: Circuit model of a generalized CPT system.

A generalized model of CPWT system is illustrated in Fig. 2.1. A high frequency inverter is used to convert DC voltage signal to a high-frequency voltage signal. The high-frequency voltage signal passes through compensation tank. It is then applied to the transmitter plates as  $V_{21}$ . Voltage  $V_{34}$  induced at the receiver side is optionally processed through a receiver compensation network and then rectified for the DC charging. In general, the compensation tank on the transmitter side act as voltage “step-up” transformer while the compensation tank on the receiver side acts as “step-down” transformer. The two most commonly used compensation networks (LC and LCL) will be analyzed in this thesis. An in-depth analysis of different compensation structures and their comparison can be found in articles [3, 20, 21]. Without losing generality, same type of compensation network will be used on both sides of the CPT system. Also, identical couplers will be used on the transmitter and receiver sides.

#### 2.2 CPT Couplers

This section provides a brief overview of different capacitive couplers. It also comments on the power density, compactness, misalignment tolerance, and application.

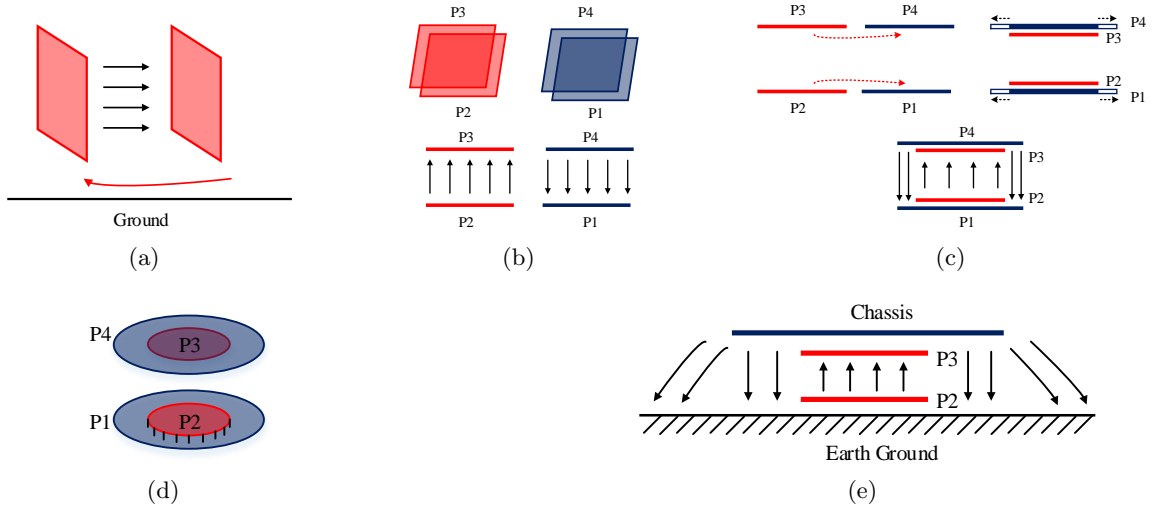


Fig. 2.2: CPT coupler types:(a) Single Wire, (b) Lateral Four-Plate, (c) Vertical Four-Plate (d) Vertical Four-Plate with circular plates (e) Vertical Four-Plate with chassis as P4 and the earth ground as P1.

### 2.2.1 Single-wire CPT couplers

Single-wire CPT utilizes only two metal plates to transfer power. It utilizes ground path and parasitic capacitance with the earth ground as the return path (Fig.2.2(a)) [22]. It is cost effective with respect to a general four plate coupler structure. It offers better misalignment and coupling tolerances. It could be used for low power applications (few watts). However, it cannot be considered in higher power practical applications as the reported efficiency and power levels were low (3.8 W and 32% ) .

### 2.2.2 Lateral CPT couplers

Lateral CPT couplers utilizes four metal plates to transfer power. It forms two pairs of coupling capacitors, as illustrated in (Fig.2.2(b)). The plates appear in pairs arranged laterally to form direct and return paths for displacement current. The two pairs should be spaced so as to minimize cross coupling capacitances. Durability, dielectric permittivity, and dielectric strength can be improved by ceramic coatings [23]. It is highly sensitive to rotational misalignment. A 180 degree rotational misalignment will make the system ineffective to transfer any power. It is the most popularly used CPT coupler.

### 2.2.3 Vertical (stacked) Four-Plate Coupler (V4PC)

Vertical (stacked) Four-Plate Coupler (V4PC) structure is proposed and analyzed in [24] and later employed for EV charging in [19]. The V4PC structure is constructed by inserting the direct path plate pair (P2 and P3) of lateral capacitor inside the P1-P4 plates of the second lateral capacitor, and extending the return path plate pairs (P1 and P4) to create a return current path, as illustrated in Fig.2.2(c). Maximum "mutual capacitance" is obtained when capacitances between plates P1-P4 and P2-P3 are approximately equal. Self-capacitances dominantly created by plates on primary (P1 and P2) and secondary sides (P3 and P4) can be used to replace or supplement critical capacitors in the primary and secondary compensation networks.

V4PC is highly tolerant to rotational misalignment. For square plates, less than 1 percent of variation of self-capacitances and less than 10 percent of variation of mutual capacitance have been reported in [19] for one complete horizontal rotation of the receiver plates with respect to the perfectly aligned position. Rotational misalignment tolerance can further be improved by replacing the square plates with circular ones Fig.2.2(d).

V4PC structure has significant unwanted cross-coupling between plates P1-P3 and P2-P4. It reduces coupling capacitance which results in reduction of power transfer density [3]. The complex cross-coupling between plates cannot be modelled analytically. Hence, Finite Element Method (FEM) modeling and analysis are used for the coupler design.

### V4PC with chassis and the earth ground

In [20, 25], authors propose replacing V4PC outer plates (P1 and P4) by the earth ground and the vehicle chassis, respectively. In these designs, the current flows forward using the coupler plates and returns to the source by utilizing parasitic capacitance's between the chassis and the earth ground, as illustrated in Fig.2.2(e). Vehicle chassis could be in a direct contact with humans. There could be safety issue if the voltage induced on vehicle chassis is significant.

## 2.3 Plate Capacitance Modelling

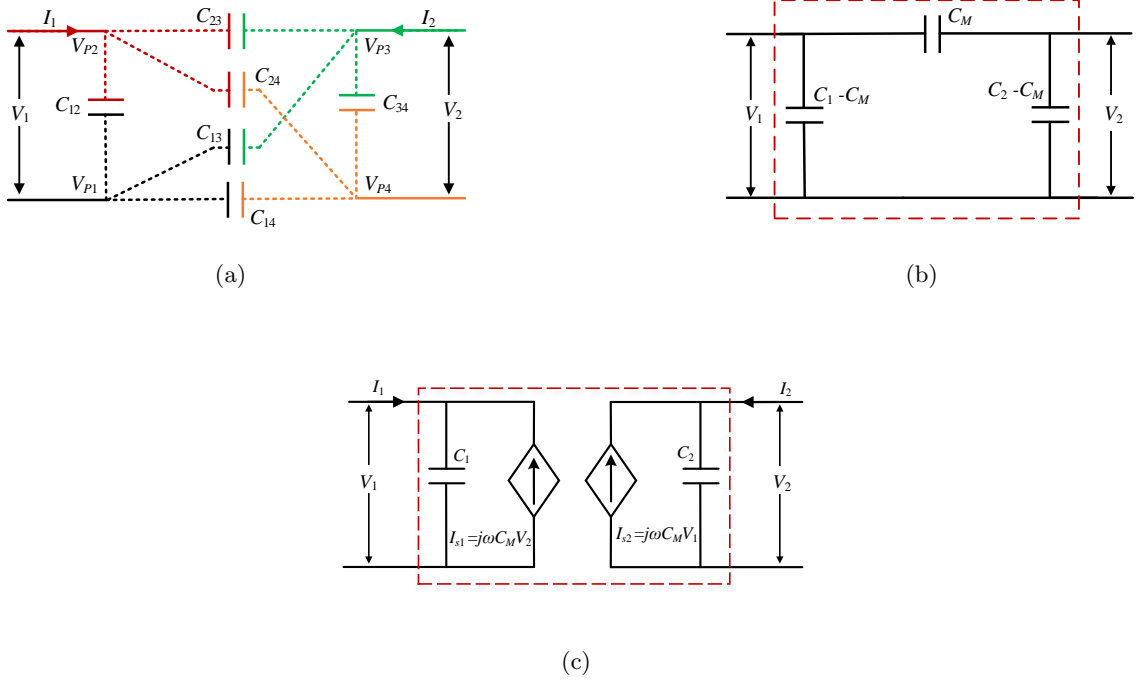


Fig. 2.3: Equivalent circuit models of a CPT coupler (a) inclusive model, (b)  $\pi$  model, and (c) behavioral model.

In V4PC design, coupling combination of four plate leads to six coupling capacitance's. All six capacitance's ( $C_{12}$ ,  $C_{13}$ ,  $C_{14}$ ,  $C_{23}$ ,  $C_{24}$ , and  $C_{34}$ ) should be considered for electric model of V4PC as the cross couplings are too significant to be neglected [19]. An inclusive model is shown in Fig.2.3(a).

The V4PC offers the advantage of higher input and output self-capacitances, dominantly created by capacitances between plates P1-P2 and P3-P4. These capacitances can be used to replace or supplement critical compensation capacitors in compensation networks, as explained in [19]. The higher the value of these input and output self-capacitances, the lower is the value of inductors required for compensation tank. At frequencies greater than 200 kHz, air-core inductores are preferred over cored inductors. The air-core inductors are of significant size as the value of inductance increases.

The initial model is transformed to a  $\pi$  model is shown in Fig.2.3(b). Finally, the coupling between the transmitter and receiver can be modeled in the form of voltage-dependent current sources. This “behavioral” model is convenient for a power flow analysis

(Fig.2.3(c)). It consists of equivalent input and output self-capacitances and dependent current sources. The equivalent behavioral model is used in this research.

## 2.4 Safety Standards and Shielding Techniques

### 2.4.1 Safety Standards

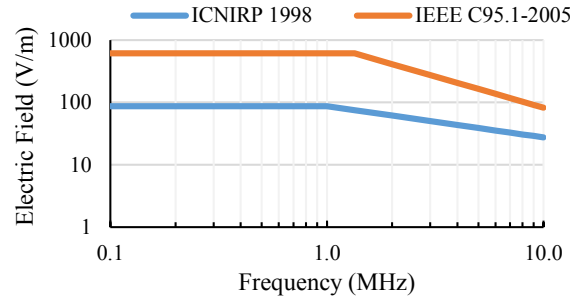


Fig. 2.4: Electric field guidelines for public exposure (ICNIRP 1998 and IEEE C95.1-2005).

Safety is the major concern when dealing with systems that produce electric or magnetic field exposure to humans. CPT is one such system which is based on electric field. Depending on the electric field frequency, the nature of interaction of an electric field with a human body changes. For lower frequencies (typically below 100 kHz) the electric field induces currents inside the body, causing functional changes in the nervous system and other tissue [26]. An exposure to high-frequency electric or magnetic fields (above 100 kHz) causes significant absorption of energy and the body temperature increases.

The allowed levels of human exposure to electric and magnetic fields are limited by regulatory standards. In the case of electric fields, there are two frequently referred exposure limits: a) IEEE C95.1-2005 standard (frequency range: 3 kHz to 300 GHz) [27], and b) International Commission on Non-Ionizing Radiation Protection (ICNIRP) recommendation ICNIRP:2009 (frequency range: 100 kHz to 300 GHz) [23]. Their limits are presented in Fig.2.4 for the frequency range 100 kHz to 10 MHz typically used in CPT systems. It can be observed that the Electric field safety limits are constant up-to 1 MHz for both the

standards. It is a challenging problem to meet these limits, particularly for increasing power requirements of modern WPT systems.

### 2.4.2 Shielding Techniques

#### Near-Field Phases-Array Cancellation

In [28], the authors proposed Near-Field Phases-Array Cancellation technique consisting of multiple phase-shifted capacitive plates to reduce the fringing field. The system is demonstrated to reduce the lateral stray field five times. The reduction in electric field is proportional to the number of phase-shifted plate-pairs. The proposed method can be applied only for lateral four plate coupler structure. Additionally, each phase-shifted plate-pair requires a dedicated inverter for operation. This increases the system cost and makes the system control complicated.

#### Six-Plate Capacitive Coupler

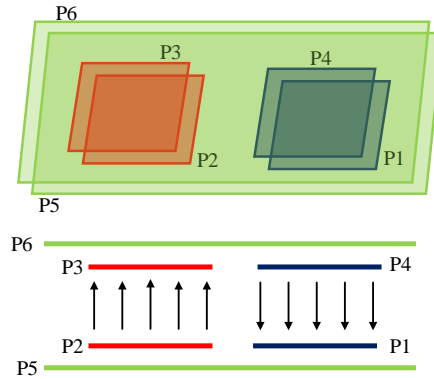


Fig. 2.5: Vertical six-plate coupler.

In [29], the authors propose a six-plate capacitive coupler (Fig.2.5) to reduce the leakage electric field. Two extra outer plates (P5 and P6) are utilized for sheilding. Through the

capacitive coupling with inner WPT plates (P1, P2, P3 and P4), the outer plates of the coupler establish ground potential between them, which effectively shield the whole system. The proposed method is also only applicable to lateral CPT couplers. In this work, the authors imply that the proposed structure is effective only for aligned pads and that the active zone around the pad increases significantly when misalignment occurs.

As both proposed methods are applicable to lateral coupler structure, there is no method developed for shielding of V4PC designs.

## 2.5 Compensation Network

In general, a CPT is characterized by low coupling capacitance (in order of few pF), which requires a large inductor for compensation on transmitter and receiver side. The addition of an external parallel capacitor reduces the value of inductance required for compensation. However, the addition of a capacitor in parallel with coupling capacitors puts constraints in terms of voltage rating. The voltage rating could be significant at higher power level (specially for EV application). Depending on the power level and coupling, a suitable compensation can be selected from L, LC, LCL and LCLC compensation network.

An in-depth analysis of different compensation structure and their comparison can be found in articles [3, 20, 21]. The most common compensation networks LC and LCL are analyzed and presented in Chapter 4. Without losing generality, it will be adopted that both sides of the system contain the same type of compensation network and that the transmitter and receiver couplers are identical.

## CHAPTER 3

## STRAY FIELD CALCULATION AND MODELLING IN CAPACITIVE COUPLERS

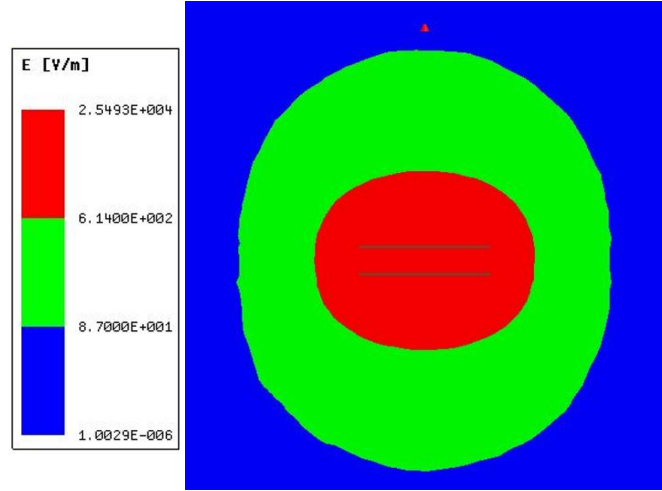


Fig. 3.1: A contour diagram showing the magnitude of the electric field strength around a two-plate coupler.

### 3.1 Active Zone Around a Circular Two-Plate Coupler

In order to illustrate the field around a typical CPT coupler, a circular two-plate coupler is modelled in an FEM simulation. The coupler is characterized by the distance between plates  $d_C$  and the radius of plate  $r_C$ . The two plates have equal radius  $r_C$ . The voltage applied across plates is 1 kV and the frequency is 250 kHz. The contour diagram of the magnitude  $E$  of the electric field vector  $\mathbf{E}$  is shown in Fig.3.1. It is a tri-color contour diagram, the red region represents an area where  $E$  exceeds the safety limit specified by IEEE C95.1-2005 standard (for frequencies below 1 MHz), the region surrounded by blue is the area where  $E$  exceeds the safety limit specified by ICNIRP 1998 standard (for frequencies below 1.34 MHz). The IEEE C95.1-2005 public safety limit for electric field exposure for



frequencies below 1 MHz is 614 V/m, while the ICNIRP 1998 public safety limit for electric field exposure for frequencies below 1.34 MHz is 85 V/m.

### 3.2 Modelling The Active Zone

It is observed from Fig.3.1 that the active zone where the field exceeds the specified limit can be approximated by an oblate or prolate spheroid described by the radius  $r_E$  and height  $h_E$ . Prolate and oblate spheroids are illustrated in Fig.3.2 with the two parameters specified.

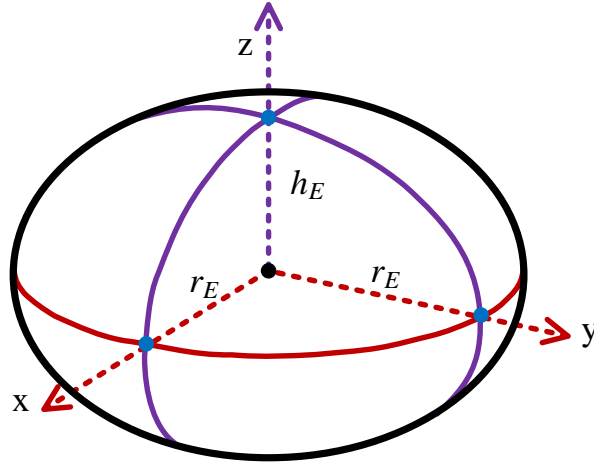


Fig. 3.2: Spheroid.

In order to quantify the electric field shielding, four parameters are introduced. Effective power density is defined as the power transferred by coupler  $P$  divided by the cross-sectional area of the active zone, as given by (3.1). Effective volumetric power density describes power  $P$  normalized by the active zone volume, as presented by (3.2). Equation (3.3) describes the area factor as the ratio between the cross-sectional areas of the active zone and coupler, while (3.4) calculates the volumetric factor as the ratio of the active zone volume and the coupler volume.

$$p_{eff} = \frac{P}{\pi r_E^2} \quad (3.1)$$

$$v_{eff} = \frac{P}{\frac{4}{3}\pi r_E^2 h_E} \quad (3.2)$$

$$F_A = \frac{\pi r_E^2}{\pi r_C^2} = \left(\frac{r_E}{r_C}\right)^2 \quad (3.3)$$

$$F_V = \frac{\frac{4}{3}\pi r_E^2 h_E}{\pi r_C^2 d_C} = \frac{4}{3} \left(\frac{r_E}{r_C}\right)^2 \frac{h_E}{d_C} \quad (3.4)$$

An ideal design of the system tends to make  $F_A$  and  $F_V$  equal to 1. Depending on the application, some parameters are more useful than others. For example, when the pads are attached to a vehicle, the stray field spreads more in lateral direction and  $p_{eff}$  and  $F_A$  are more relevant in that case. As an illustration, parameters of the system in Fig.3.1 are calculated and presented in Table 3.1, considering  $V_0=1$  kV and  $f_s=250$  kHz. For the given example, the volume of the active zone is 79 times larger than the physical coupler volume when the field is limited to 87 V/m and that number reduces to 11.8 when the field is allowed to reach 614 V/m.

Table 3.1: Coupler specifications and parameter values

$r_C$		25 cm	
$d_C$		10.7 cm	
$r_i$		21.1 cm	
$d_i$		0.6 cm	
Parameters	Value	Parameters	Value
$r_{E,87}$	70 cm	$r_{E,614}$	41.5 cm
$h_{E,87}$	78.7 cm	$h_{E,614}$	33.7 cm
$F_{P,87}$	7.84	$F_{P,614}$	2.75
$F_{V,87}$	79	$F_{V,614}$	11.8

### 3.3 Active Zone Calculation

The authors in [30, 31] derive analytical equations to calculate potential  $V$  around a circular two-plate capacitive coupler. At an arbitrary point described by cylindrical

coordinates  $\rho$  and  $z$ , measured with respect to the center of the coupler,  $V$  can be calculated as:

$$V(\rho, z) = \frac{V_0}{2\pi} \operatorname{Re} \left( \int \left( \frac{1}{[\rho^2 + (z - 0.5h_C + jx)^2]^{1/2}} - \frac{1}{[\rho^2 + (z + 0.5h_C + jx)^2]^{1/2}} \right) f(x) dx \right) \quad (3.5)$$

where  $V_0$  is the voltage between plates (with the top plate being a positive one),  $x$  is the integration variable, and  $f(x)$  is the solution of the integral :

$$f(y) - \frac{h_C}{r_C \pi} \int_{-1}^1 \frac{f(x) dx}{\left(\frac{h_C}{r_C}\right)^2 + (y - x)^2} = 1 \quad (3.6)$$

$f(x)$  can be solved by the finite difference method [32], or iteratively by adopting  $f(x)=1$  as an initial guess. If the iterative method is adopted, after  $f(y)$  is calculated from (3.6), it is reassigned to  $f(x)$  at the beginning of next iteration to calculate new  $f(y)$ . After enough iterations,  $f(y)$  stops changing, it becomes  $f(x)$ , and it is ready for  $V$  calculation in (3.5). Each coupler specified by  $r_C$  and  $h_C$  has one associated  $f(x)$ . Iterative method is utilized in the paper to solve for  $f(x)$ .

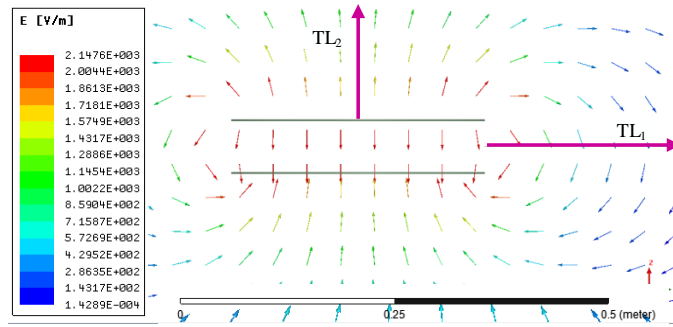


Fig. 3.3: Test lines for electric field measurement.

Due to coupler symmetry, electric field strength  $E$  along the lines of interest (TL<sub>1</sub> and TL<sub>2</sub> in Fig.3.3) has only vertical component, which can be calculated by using the derivative

of 3.5 with respect to  $z$ :

$$E_V(\rho, z) = \frac{dV(\rho, z)}{dz} \quad (3.7)$$

$$E_V(\rho, z) = \frac{V_0}{2\pi} \operatorname{Re} \left( \int \left( \frac{z + 0.5h_C + jx}{[\rho^2 + (z + 0.5h_C + jx)^2]^{3/2}} - \frac{z - 0.5h_C + jx}{[\rho^2 + (z - 0.5h_C + jx)^2]^{3/2}} \right) f(x) dx \right) \quad (3.8)$$

Along the horizontal line  $z=0$ ,  $E$  will be:

$$E_{z=0} = \frac{V_0}{2\pi} \operatorname{Re} \left( \int \left( \frac{0.5h_C + jx}{[\rho^2 + (0.5h_C + jx)^2]^{3/2}} + \frac{0.5h_C - jx}{[\rho^2 + (0.5h_C - jx)^2]^{3/2}} \right) f(x) dx \right) \quad (3.9)$$

Similarly, along the vertical line where  $\rho=0$ , the electric field strength is:

$$E_{\rho=0} = \frac{V_0}{2\pi} \operatorname{Re} \left( \int \left( \frac{1}{(z + 0.5h_C + jx)^2} - \frac{1}{(z - 0.5h_C + jx)^2} \right) f(x) dx \right) \quad (3.10)$$

By equating 3.9 and 3.10 with  $E_m a x$ , one can obtain the boundaries  $r_E$  and  $h_E$  of the active zone:

$$\frac{2\pi E_{\max}}{V_0} = \operatorname{Re} \left( \int \left( \frac{0.5h_C + jx}{[r_C^2 + (0.5h_C + jx)^2]^{3/2}} + \frac{0.5h_C - jx}{[r_C^2 + (0.5h_C - jx)^2]^{3/2}} \right) f(x) dx \right) \quad (3.11)$$

$$\frac{2\pi E_{\max}}{V_0} = \operatorname{Re} \left( \int \left( \frac{1}{(h_C + 0.5h_C + jx)^2} - \frac{1}{(h_C - 0.5h_C + jx)^2} \right) f(x) dx \right) \quad (3.12)$$

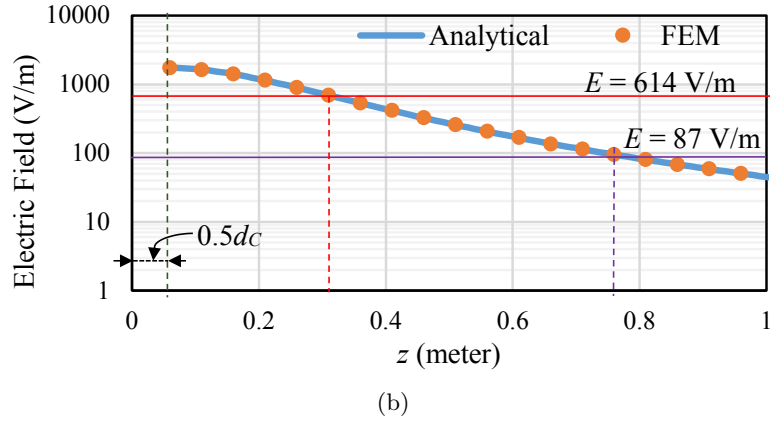
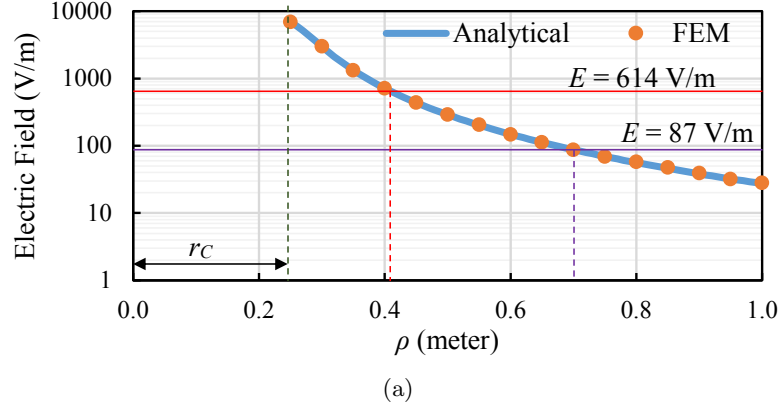


Fig. 3.4: Electric field calculated and simulated along the test lines (a)  $TL_1$  and (b)  $TL_2$  .

The described procedure is applied to the coupler specified in TABLE 3.1 and the results are presented to show the field on  $TL_1$  (Fig.3.4(a)) and  $TL_2$  (Fig.3.4(b)) test lines, starting from the edge of the coupler. The field levels allowed by IEEE and ICNIRP standards for  $f < 1$  MHz are specified by horizontal lines. For verification of the analytical method, the same figure presents the field level obtained from FEM simulations, too. Very good matching between two curves justifies the use of analytical approach in calculating the active zone boundaries.

### 3.4 Active zone around a V4PC

Considering that V4PC has two additional plates, it is important to investigate if the approach from Section 3.3 can be utilized to study the active zone around a V4PC, too. In a well design CPT system containing a V4PC, capacitances between plates P2-P3 and P1-P4

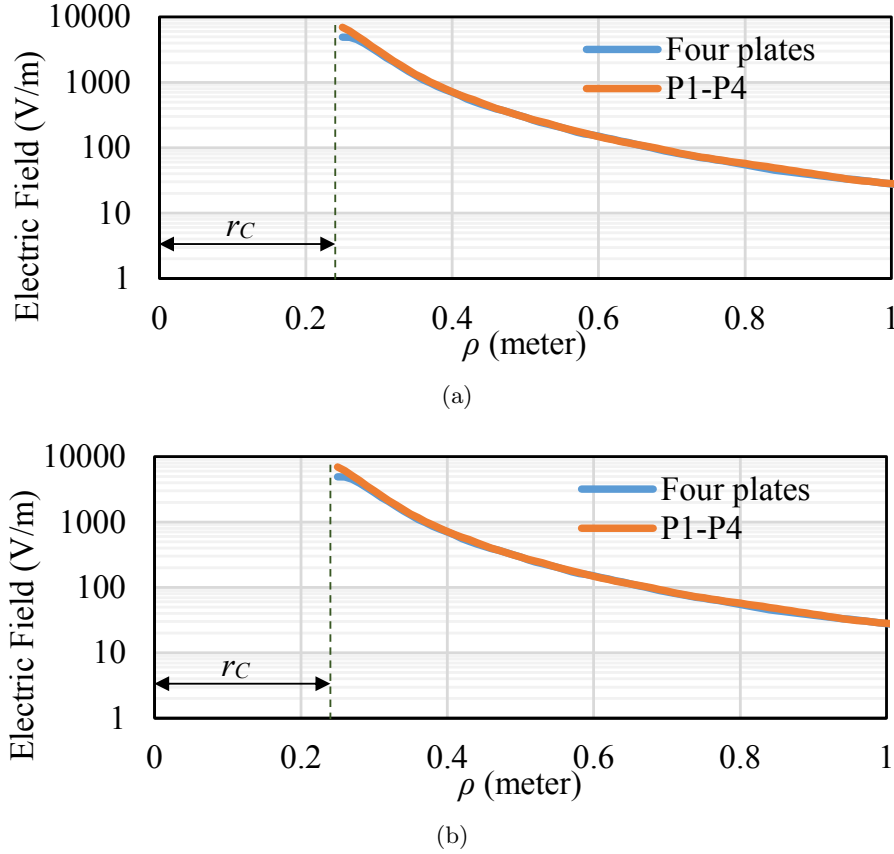


Fig. 3.5: An electric field simulated for four-plate and two-plate couplers along the test lines (a)  $TL_1$  and (b)  $TL_2$ .

are close in value. Since P2-P3 dominantly conducts the direct path current and since the same return path current mostly flows through P4-P1, one can conclude that the voltages between palates 2-3 and 4-1 are similar:  $V_{23} \approx V_{41}$ . Two FEM simulations are conducted to compare the impact of inner plates P2 and P3 on the size of an active zone. In the first simulation, all four plates are modeled and voltages  $V_{23}=V_{41}=1$  kV are assigned to them. As seen in Fig.3.5(a) and Fig.3.5(b), the field along  $TL_1$  and  $TL_2$  is almost identical in these two cases, with the only divergence identified at the coupler edge along  $TL_1$ . That implies that plates P2 and P3, as being imbedded in the coupler and far from the couplers edge, have a marginal impact on the size of the active zone.

The presented results lead to an important conclusions that for low and medium gaps between plates i) the same procedure described in Section 3.3 can be applied to calculate

the parameters of the active zone around a V4PC, and ii) the voltage between plates P1 and P4 ( $V_{14}$ ) dominantly determines the size and the shape of the active zone around the coupler. Considering that there is no effective shielding method for V4PC proposed so far, it is essential to explore how the design of compensation network at the transmitter and the receiver can reduce the size of the active zone, while still delivering the same power. In the next section, two frequently used compensation network, LC and LCL, will be explored and the optimum design of compensation elements will be derived to reduce the size of the active zone.

## CHAPTER 4

### OPTIMUM DESIGN OF COMPENSATION CIRCUIT FOR MINIMUM ACTIVE ZONE

#### 4.1 Double-sided LC Compensation

A CPT system with LC compensation networks at the transmitter and receiver is shown in Fig.4.1(a). In Fig.4.1(b), a simplified model is presented in which the input inverter is replaced by a controlled *ac* source  $V_{inv}$ , the rectifier and the output battery are replaced with an equivalent *ac* resistance  $R_{ac,eq}$  and a simplified two-port model from Fig.2.3(c) is used instead of the V4PC physical model. The LC networks consist of series transmitter and receiver inductors ( $L_1$  and  $L_2$ ) and external shunt capacitors ( $C_{1,ext}$  and  $C_{2,ext}$ ). The presence of  $C_{1,ext}$  and  $C_{2,ext}$  helps to decrease the value of compensation inductances  $L_1$  and  $L_2$ , to boost the output power, and prevents an excessive detuning in a misalignment case. The reactance of  $L_2$  is tuned to match the reactance of the receiver input capacitance  $C_2 + C_{2,ext}$  and the reactance of  $L_1$  is tuned to match the combined reactances of the transmitter input capacitance  $C_1 + C_{1,ext}$  and the reflected secondary capacitance  $-C_M^2/(C_2 + C_{2,ext})$ :

$$\omega_s^2 L_2 (C_2 + C_{2,ext}) = 1 \quad (4.1)$$

$$\omega_s^2 L_1 \left( C_1 + C_{1,ext} - \frac{C_M^2}{C_2 + C_{2,ext}} \right) = 1 \quad (4.2)$$

The Norton theorem can be applied to derive the transmitter equivalent circuit referred to the receiver, as shown in Fig.4.2. Equivalent Norton current source  $\mathbf{I}_N$  and equivalent admittance  $\mathbf{Y}_N$  are obtained as:

$$\mathbf{I}_N = -j\omega_s \frac{(C_2 + C_{2,ext})}{C_M} \left( C_1 + C_{1,ext} - \frac{C_M^2}{C_2 + C_{2,ext}} \right) \mathbf{V}_{inv} \quad (4.3)$$



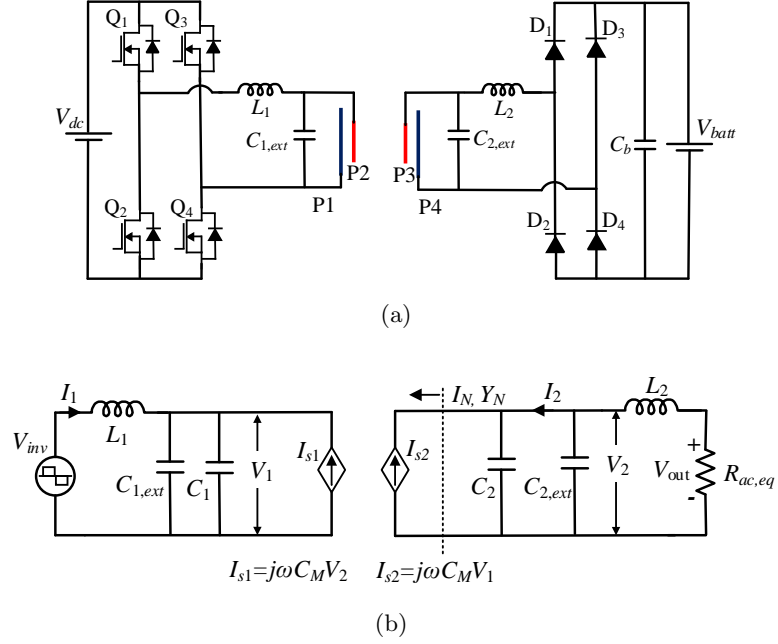


Fig. 4.1: a) A CPT system with LC compensation networks and (b) its simplified functional model.

$$\mathbf{Y}_N = -j\omega_s (C_2 + C_{2,ext}) \quad (4.4)$$

Taking into account the anti-resonance between  $\mathbf{Y}_N$  and capacitors  $C_2$  and  $C_{2,ext}$ , the output power can be calculated using (4.3) as:

$$P_{out} = \frac{\omega_s V_{out} V_{inv}}{C_M} \left( C_1 + C_{1,ext} - \frac{C_M^2}{C_2 + C_{2,ext}} \right) (C_2 + C_{2,ext}) \quad (4.5)$$

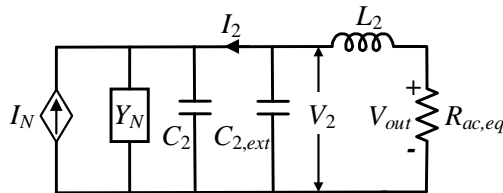


Fig. 4.2: The Norton equivalent circuit of the transmitter side referred to the receiver.

As can be seen, by adding the external capacitances, the output power increases. For

specified  $V_{out}$  and  $V_{in}$  and for a known coupler  $C_1$ ,  $C_2$  and  $C_M$ , capacitances  $C_{1,ext}$  and  $C_{2,ext}$  can be designed to achieve the requested output power  $P_{out}$ . After  $P_{out}$  is set to its expected value, the extra degree of freedom can be utilized to reduce voltage  $V_{14}$ , and that way to reduce the size of the active zone. The expression of phasor  $\mathbf{V}_{14}$  is derived in [19] as:

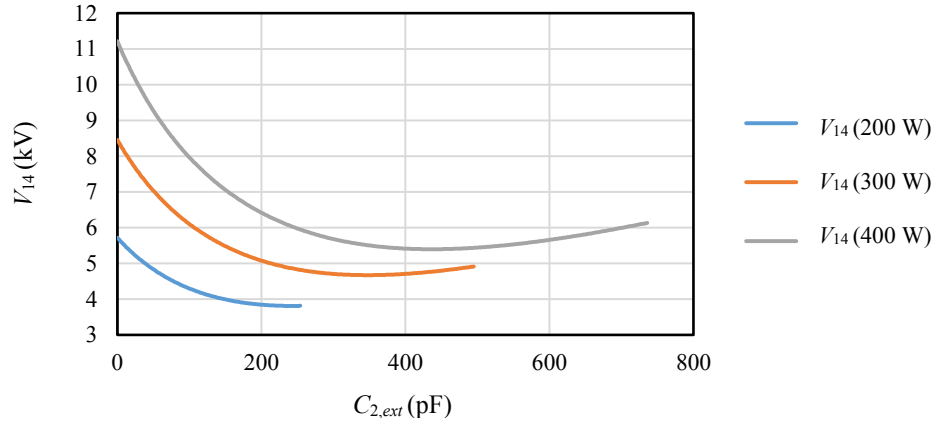


Fig. 4.3: The magnitude of  $V_{14}$  for different compensation capacitance  $C_{2,ext}$  and three different power ratings  $P_{out}$ .

$$\mathbf{V}_{14} = -\frac{\mathbf{I}_2}{j\omega_s C_X} + \alpha_c \mathbf{V}_2 \quad (4.6)$$

where  $C_X$  and  $\alpha_c$  depend on couplers parameters:

$$C_X = \frac{C_{14}C_{23} - C_{24}C_{13}}{C_{24} + C_{23}} \quad (4.7)$$

$$\alpha_c = \frac{C_{34}(C_{24} + C_{23}) + C_{24}(C_{13} + C_{23})}{C_{14}C_{23} - C_{24}C_{13}} \quad (4.8)$$

From Fig.4.1(b),  $\mathbf{I}_2$  can be written as:

$$\mathbf{I}_2 = -j\omega_s C_{2,ext} \mathbf{V}_2 - \mathbf{I}_N; \quad (4.9)$$

Since:

$$\mathbf{V}_2 = \mathbf{I}_N (j\omega_s L_2 + R_{ac,eq}); \quad (4.10)$$

one can combine (4.1), (4.8), (4.9) and (4.10) to derive an expression for  $\mathbf{V}_{14}$ :

$$\mathbf{V}_{14} = \frac{P_{out}}{V_{out}} \frac{\left(\alpha_c - \frac{C_2}{C_X}\right)}{\omega_s (C_2 + C_{2,ext})} - jV_{out} \left(\frac{C_{2,ext}}{C_X} + \alpha_c\right); \quad (4.11)$$

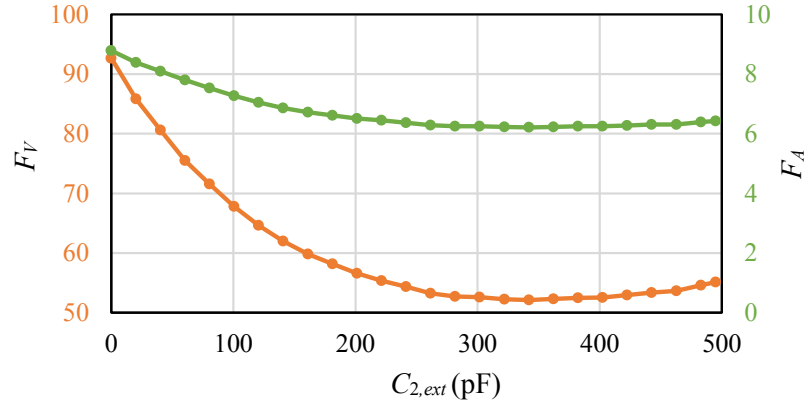


Fig. 4.4: The impact of the capacitor selection on the  $F_A$  and  $F_V$  ( $V_{inv}$ =100 V,  $V_{out}$ =50 V, and  $P_{out}$ =300 W).

Table 4.1: System specifications

Parameters	Value	Parameters	Value
$V_{inv}$	100 V	$V_{out}$	50 V
$f_s$	250 kHz		
$C_{12}$	222.73 pF	$C_{23}$	11.38 pF
$C_{13}$	2.63 pF	$C_{24}$	2.72 pF
$C_{14}$	11.36 pF	$C_{34}$	221 pF
Equivalent coupler capacitances			
$C_1$	229.75 pF	$C_2$	228.02 pF
$C_M$	4.35 pF		

Where  $R_{ac,eq}$  is replaced by  $(V_{out})^2/P_{out}$ . For the system specifications given in TABLE 4.1,

the impact of  $C_{2,ext}$  is explored by varying  $C_{2,ext}$  in small steps for three different power ratings ( $P_{out}=200$  W, 300W, and 400 W), and plotting the  $V_{14}$  magnitude in Fig.4.3. As the output power increases, more pairs of capacitances  $C_{1,ext}$  and  $C_{2,ext}$  satisfies (4.5) , causing the curve for  $P_{out}=400$  W to be longer than those for  $P_{out}=100$  W or  $P_{out}=200$  W. Additionally, the results clearly illustrate the existence of a minimum of  $V_{14}$  for a particular pair of  $C_{1,ext}$  and  $C_{2,ext}$  capacitors. For example, the difference between the optimum and the worst pair of capacitances in terms of  $V_{14}$  and for  $P_{out}=400$  W is 51.9(%). Fig. 4.4 illustrates the impact of the capacitor selection on areal and volumetric factors  $F_A$  and  $F_V$  showing that a proper selection can reduce  $F_A$  by 29.3%and  $F_V$  for 44.9% (from 92.7 coupler sizes to 52.1).

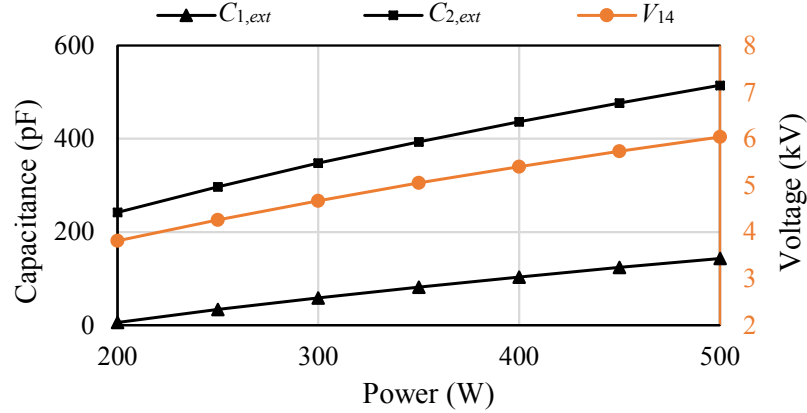


Fig. 4.5: Optimum compensation pairs  $C_{1,ext,opt}$  and  $C_{2,ext,opt}$  and optimum voltage  $V_{14}$  as a function of  $P_{out}$ .

In order to calculate the optimum capacitor pair, the magnitude of  $V_{14}$  is derived from (3.5), then differentiated with respect to  $C_{2,ext}$ , and finally the derivative is equated to zero, resulting in a fifth-order equation:

$$a_5 C_{2,ext}^5 + a_4 C_{2,ext}^4 + a_3 C_{2,ext}^3 + a_2 C_{2,ext}^2 + a_1 C_{2,ext} + a_0 = 0 \quad (4.12)$$

where the expressions of coefficients  $a_0$  to  $a_5$  are summarized in TABLE 4.2.

By solving (4.12), an optimum selection of  $C_{2,ext,opt}$  for minimum  $C_{V,14}$  can be obtained.

Table 4.2: System specifications

Coefficients	Expression	Coefficients	Expression
$a_0$	$C_2^5 \left( \alpha_{CX2} - \frac{P_{out}^2}{V_{out}^4 \omega^2 C_2^2} (1 - \alpha_{CX2})^2 \right)$	$a_3$	$C_2^2 (6 + 4\alpha_{CX2})$
$a_1$	$C_2^4 \left( 4\alpha_{CX2} + 1 - \frac{P_{out}^2}{V_{out}^4 \omega^2 C_2^2} (1 - \alpha_{CX2})^2 \right)$	$a_4$	$C_2 (\alpha_{CX2} + 4)$
$a_2$	$C_2^3 (4 + 6\alpha_{CX2})$	$a_5$	1
$\alpha_{CX2} = \alpha_C \frac{C_X}{C_2}$			

From TABLE 4.2, one can see that  $C_{2,ext,opt}$  depends on  $P_{out}$  and  $V_{out}$ , and it is independent on  $V_{inv}$ . Optimum  $C_{1,ext,opt}$  is then obtained from (4.5) as:

$$C_{1,ext,opt} = \frac{C_M}{C_2 + C_{2,ext,opt}} \left( \frac{P_{out}}{\omega V_{out} V_{inv}} + C_M \right) - C_1 \quad (4.13)$$

Fig.4.5 describes how the optimum compensation pair changes for different power levels demonstrating an almost linear dependence between  $V_{14}$  and  $P_{out}$ . In Fig.4.7 and Fig.4.6, the input and output voltages are varied and optimum  $C_{1,ext,opt}$  and  $C_{2,ext,opt}$  are calculated. As expected,  $C_{2,ext,opt}$  stays constant when  $V_{inv}$  varies, while very small variation (less than 1%) is observed in  $C_{1,ext,opt}$  when  $V_{out}$  changes. This discrepancy is caused by different compensations at the transmitter and receiver since the transmitter compensation takes into account the reflected negative capacitance  $(C_M)^2/(C_2 + C_{2,ext})$ , but the receiver compensation does not. Considering that  $(C_M)^2/(C_2 + C_{2,ext}) \ll C_1 + C_{1,ext}$ , the difference is insignificant and will be neglected in the analysis below. The minimum  $V_{14}$  demonstrates almost no change with  $V_{inv}$  and  $V_{out}$ .

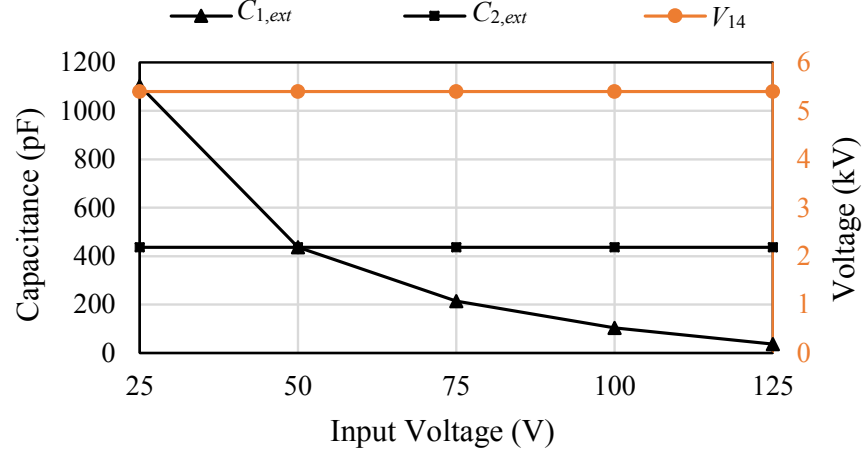


Fig. 4.6: Optimum compensation pairs  $C_{1,ext,opt}$  and  $C_{2,ext,opt}$  and optimum voltage  $V_{14}$  as a function of  $V_{inv}$ .

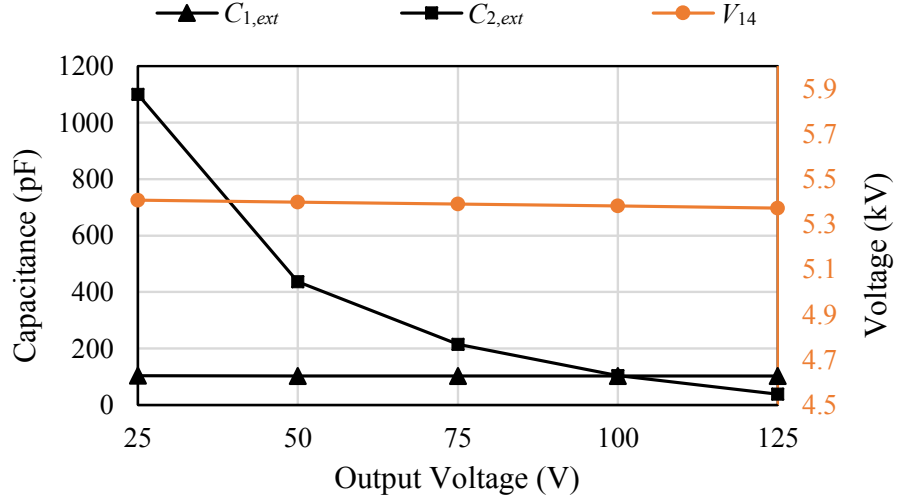


Fig. 4.7: Optimum compensation pairs  $C_{1,ext,opt}$  and  $C_{2,ext,opt}$  and optimum voltage  $V_{14}$  as a function of  $V_{out}$ .

$C_{2,ext,opt}$  being independent on  $V_{inv}$  allows a simple calculation procedure for the broad category of symmetric couplers to be developed. Symmetric couplers can be described by  $C_{12} = C_{34}$ ,  $C_{13} = C_{24}$ , and  $C_{14} = C_{23}$ , which results in  $C_1 = C_2$ , too. For a symmetric coupler, and for identical input and output voltages  $V_{inv} = V_{out}$ , due to the symmetrical CPT structure, it is justifiable to adopt that  $C_{1,ext,opt}$  and  $C_{2,ext,opt}$  are identical. That allows  $C_{2,ext,opt}$  to be calculated from (4.5) adopting that  $V_{inv} = V_{out}$  and that  $C_1 + C_{1,ext}$  is the same as  $C_1 + C_{1,ext,opt}$ :

$$C_{2,ext,opt} = \sqrt{C_M \left( \frac{P_{out}}{\omega V_{out}^2} + C_M \right)} - C_2 \quad (4.14)$$

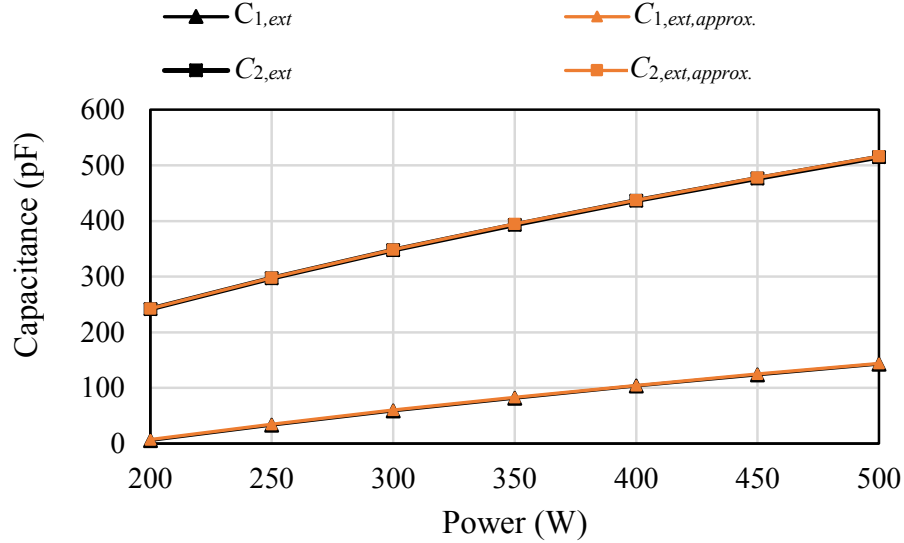


Fig. 4.8: Comparison of optimum capacitances  $C_{1,ext,opt}$  and  $C_{2,ext,opt}$  for a symmetric coupler obtained by using eqn. (4.12) vs. (4.14).

After  $C_{2,ext,opt}$  is calculated, (4.13) should be applied to get  $C_{1,ext,opt}$ . To illustrate the accuracy of the simplified approach,  $C_{1,ext,opt}$  and  $C_{2,ext,opt}$  are calculated using the approximate method, and plotted in Fig. 4.5 together with the results obtained from (4.10) and (4.13). As seen, no significant divergence is identified between two procedures for the

given power range and the coupler specified in TABLE 4.2. Maximum difference between capacitance values of 1.5 pF is identified for 200 W, and it drops to 1 pF at 500 W. The error is mostly caused by the slight asymmetry of the coupler in TABLE 4.2.

## 4.2 Double-sided LCL Compensation

With respect to the LC compensation, the LCL compensation introduces a new filtering pair  $L_{f1}-C_{f1}$  and  $L_{f2}-C_{f2}$  at the transmitter and the receiver, respectively, but eliminates the critical parallel capacitors  $C_{1,ext}$  and  $C_{2,ext}$ . The simplified functional model of an LCL compensated CPT is presented in Fig.4.9 with the magnetic coupler replaced by the behavioral model from Fig.2.3(c).

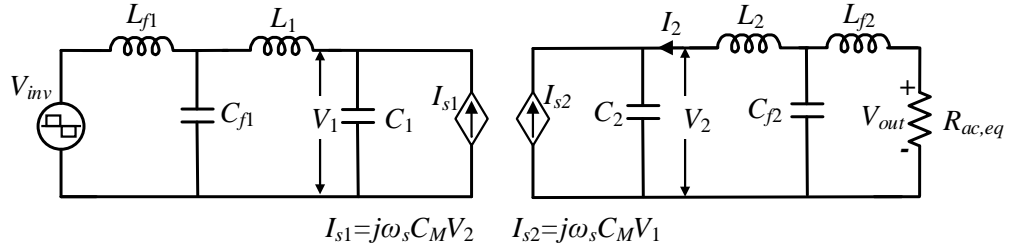


Fig. 4.9: The simplified functional model of an double-sided LCL compensated CPT.

When the tuning condition (4.15)-(4.17) are satisfied, the expression for the power transfer of a lossless LCL CPT is given by (4.18) [19]:

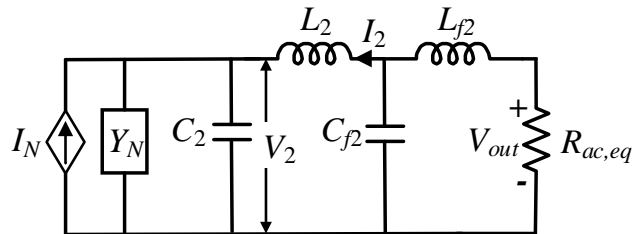


Fig. 4.10: The Norton equivalent circuit of the transmitter side referred to the receiver.



$$\omega_s^2 L_{f1} C_{f1} = \omega_s^2 L_{f2} C_{f2} = 1 \quad (4.15)$$

$$\omega_s L_1 = \frac{1}{\omega_s C_{f1}} + \frac{C_2}{\omega_s (C_2 C_1 - C_M^2)} \quad (4.16)$$

$$\omega_s L_2 = \frac{1}{\omega_s C_{f2}} + \frac{C_1}{\omega_s (C_2 C_1 - C_M^2)} \quad (4.17)$$

$$P_{out} = \frac{\omega_s C_M V_{inv} V_{out}}{C_1 C_2 - C_M^2} C_{f1} C_{f2} \quad (4.18)$$

If the Norton theorem is applied in the similar fashion as in Section 4.1, the secondary circuit can be redrawn as presented in Fig.4.10, where the Norton current source and admittance are expressed as:

$$P_{out} = \frac{\omega_s C_M V_{inv} V_{out}}{C_1 C_2 - C_M^2} C_{f1} C_{f2} \quad (4.19)$$

$$\mathbf{I}_N = -j\omega_s \frac{C_M C_{f1} V_{inv}}{C_1} \quad (4.20)$$

$$\mathbf{Y}_N = -j\omega_s \frac{C_M^2}{C_1} \quad (4.21)$$

Using Fig.4.10, the coupler output voltage and current phasors  $\mathbf{I}_2$  and  $\mathbf{V}_2$  can be expressed as:

$$\mathbf{I}_2 = \omega_s V_{out} C_{f2} \angle 0^\circ \quad (4.22)$$

$$\mathbf{V}_2 = -\frac{P_{out}}{\omega_s C_{f2} V_{out}} - j \frac{C_1 C_{f2}}{(C_1 C_2 - C_M^2)} V_{out} \quad (4.23)$$

After replacing (4.22) and (4.23) into (4.6), the expression for  $V_{14}$  is derived as:

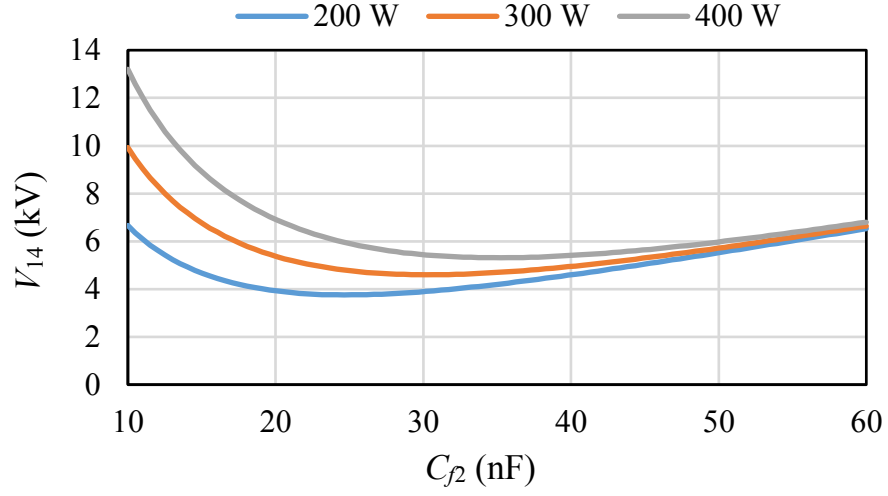


Fig. 4.11: The magnitude of  $V_{14}$  for different  $C_{f2}$  and three different power ratings  $P_{out}$ .

$$V_{14} = -\frac{\alpha_C P_{out}}{\omega_s V_{out}} \frac{1}{C_{f2}} + jV_{out} \left( \frac{1}{C_X} - \frac{\alpha_C C_1}{(C_1 C_2 - C_M^2)} \right) C_{f2} \quad (4.24)$$

Applying a similar method of finding minimum based on derivatives as in Section 4.1, an optimum capacitance  $C_{f2,opt}$  can be derived in an explicit form as:

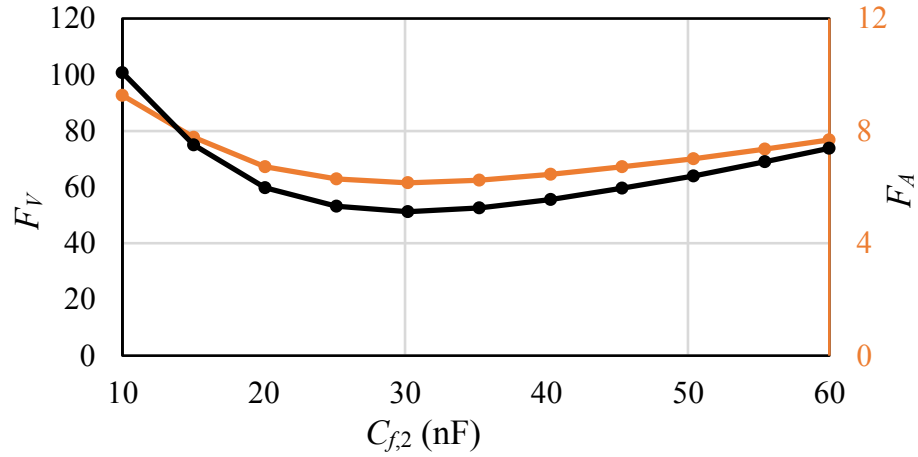


Fig. 4.12: The impact of the capacitor selection on the  $F_V$  and  $F_A$  factors ( $P_{out}=300$  W).

$$C_{f2,opt} = \frac{1}{V_{out}} \sqrt{\frac{\alpha_C P_{out} C_X (C_1 C_2 - C_M^2)}{\omega_s (C_1 C_2 - C_M^2 - \alpha_C C_1 C_X)}} \quad (4.25)$$

Optimum capacitance  $C_{f2,opt}$  is then calculated to satisfy the power requirement (4.19) as:

$$C_{f1,opt} = \frac{\sqrt{P_{out} (C_1 C_2 - C_M^2) (C_1 C_2 - C_M^2 - k_C C_1 C_X)}}{V_{inv} C_M \sqrt{\omega_s \alpha_C C_X}} \quad (4.26)$$

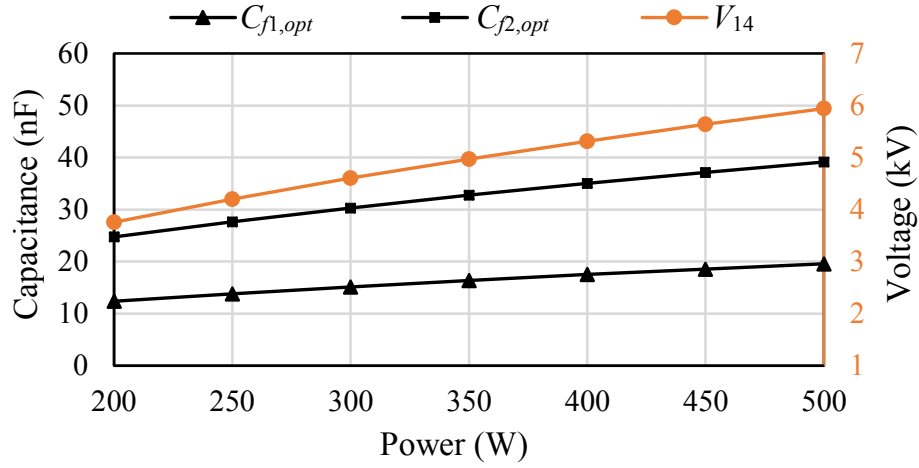


Fig. 4.13: Optimum  $C_{f1,opt}$  and  $C_{f2,opt}$  and optimum voltage  $V_{14}$  as a function of  $P_{out}$ .

As seen from (4.26),  $C_{f2,opt}$  does not depend on  $V_{inv}$  and it is inversely proportional to  $V_{out}$ . Similarly from (4.26),  $C_{f1,opt}$  does not depend on  $V_{out}$  but it is inversely dependent on  $V_{inv}$ . The curves in Fig.4.11 demonstrate the existence of optimum  $C_{f1,opt}$  and  $C_{f2,opt}$  when the power varies from 200 W to 400 W in the system depicted in Table 4.1. Fig.4.12 illustrates the impact of the capacitor selection on areal and volumetric factors  $F_A$  and  $F_V$ . Increasing the capacitances beyond the optimum values would make the active zone larger but it can be beneficial from the perspective of reducing the size of inductors  $L_{f,1}$ ,  $L_{f,2}$ ,  $L_1$ , and  $L_2$ . Fig.4.13 shows that  $V_{14}$  increases with power from 3.76 kV for  $P_{out}=200$  W to  $V_{14}=5.94$  kV for  $P_{out}=500$  W. One can observe very similar values of minimum voltage  $V_{14,opt}$  for double-sided LC (Fig.4.5) and double-sided LCL (Fig.4.13) topologies (difference less than 2%). That might be an indication that, if optimally set, the type of compensation

network has no impact on the active zone size. However, more research is needed to study the correlation between the type of the compensation network and the minimum size of the active zone.

## CHAPTER 5

### PRACTICAL CONSIDERATIONS OF AN V4PC IMPLEMENTATION

As evident from Chapter 4, the stray electric field can be a significant barrier toward practical implementation of V4PCs. To reduce the size of the active zone, two methods are considered for V4PC systems so far: a) the extension of the outer plates P1 and P4, and b) the addition of shielding plates P5 and P6. These two methods are illustrated in Fig.5.1 and will be studied below in the light of optimum designs derived in Chapter 4.

#### 5.1 Design with Extended Outer Plates

Practical implementation of the first method is proposed in [20] where the earth ground and the vehicle chassis are employed as plates P1 and P4, respectively. The authors derived that the voltage  $V_{12}$  is directly proportional to the ratio  $(C_{23})^{0.5}/C_{14}$ , from where they propose using the earth ground as plate P1 and the chassis as plate P4, and utilizing stray capacitance between the chassis and the ground as the return current path. The chassis and the earth ground maximize the size of  $C_{14}$  and provide the best ratio between  $C_{14}$  and  $C_{23}$ . The optimization procedure presented in Chapter 4 can enhance the results from [20] by actually providing the tool to calculate the minimum voltage of the chassis.

Considering the V4PC described in TABLE 4.1 and the double-sided LCL compensation, the size of plates P1 and P4 is uniformly increased to study the impact of their diameter  $r_o$  on  $V_{14,opt}$  and the size of the active zone. Fig.5.2 presents the optimum values of  $V_{14,opt}$ , radius  $r_{E,opt}$  and height  $h_{E,opt}$  of the active zone spheroid. The ratio between the size of the active zone for an arbitrary diameter  $r_o$  normalized by the size of the active zone for  $r_o=50$  cm (the case specified in TABLE 4.1), are presented in Fig.5.3.  $r_{E,opt}$  and  $h_{E,opt}$  are obtained from FEM simulations, but they can be equally calculated using (3.11) and (3.12). In case when the earth ground is used as P1, then the method of images needs to be applied first to remove the ground plate, followed by (3.11) and (3.12) applied on plates

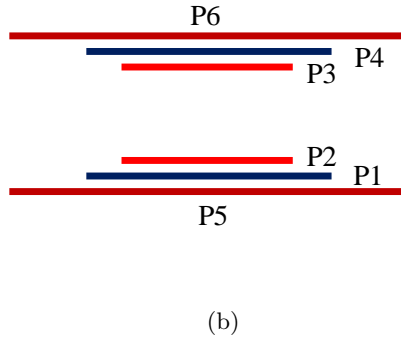
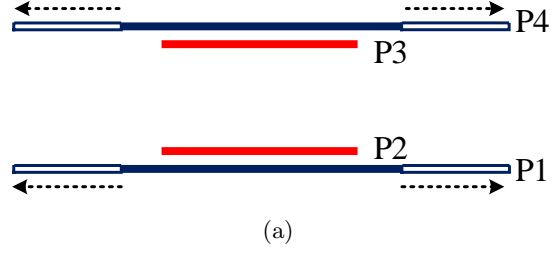


Fig. 5.1: A V4PC with a) extended outer plates, b) shielding plates P5 and P6.

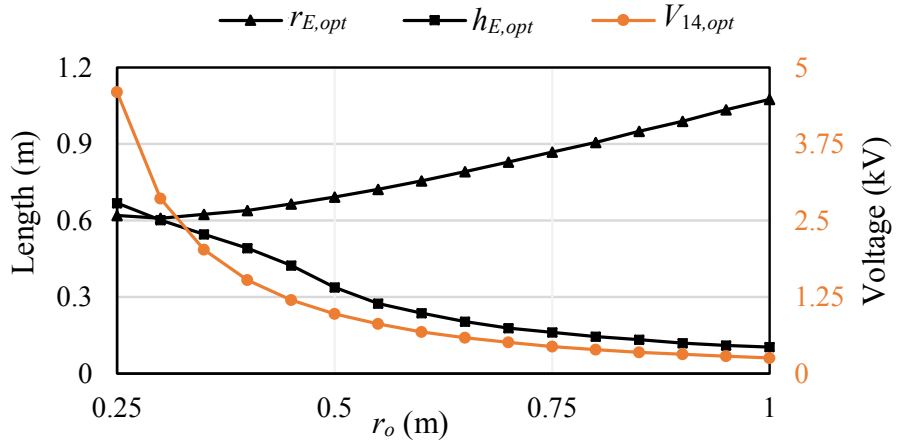


Fig. 5.2: The optimum values of  $V_{14,opt}$ , radius  $r_{E,opt}$  and height  $h_{E,opt}$  of the active zone spheroid.

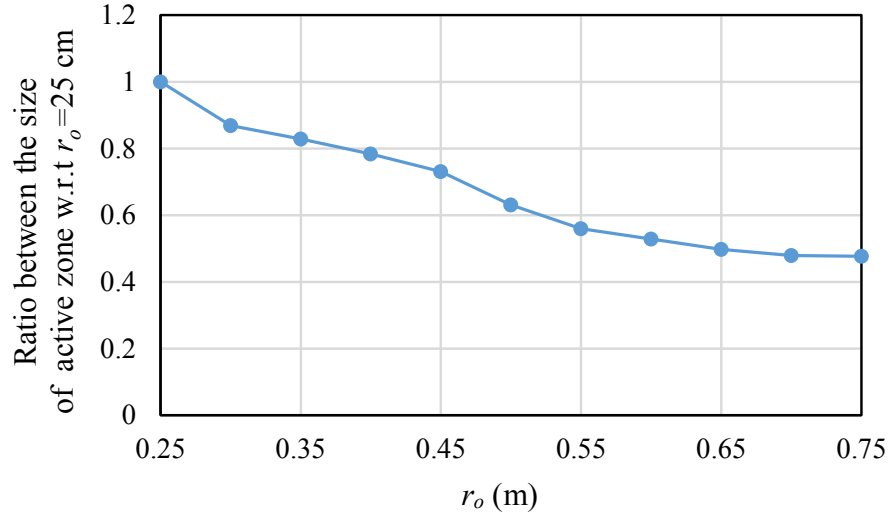


Fig. 5.3: The ratio between the size of active zone for an arbitrary radius  $r_o$ , and active zone for minimum  $r_o = 25$  cm ( $P_{out} = 300$  W).

P4 and its mirrored plate. As seen from Fig. 5.2, the voltage  $V_{14}$  decreases significantly with the increase of plates size, but the size of the active zone reduces much slower due to the increase of the coupler itself. For large plates and low voltage  $V_{14}$ , that active zone loses its characteristic spherical shape, with the maximum field being detected near the edge of the couplers, as illustrated in Fig. 5.4.

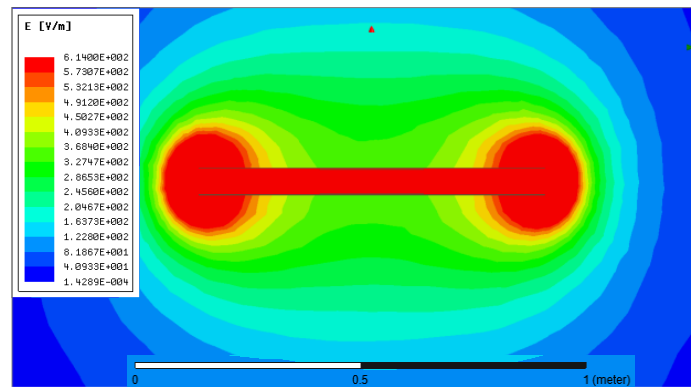


Fig. 5.4: Distorted magnetic field contour at low voltage  $V_{14}$ .

Finally, the impact of inner plates is explored by varying the size of P2 and P3 while

maintaining  $r_o=0.75$  m and the value of  $V_{14}$  is presented in Fig.5.5. From the standpoint of the minimum active zone, smaller plates P2 and P3 are preferred, which confirms the conclusion in [20]. On the other hand, the  $r_i$  reduction causes  $V_{12}$  and  $V_{34}$  to increase significantly, and a compromise is needed.

Although this design effectively uses the chassis and the earth ground reducing the number of the coupler plates, the voltage between the chassis and the ground can be unsafe for humans to touch, requesting the chassis to be made of multiple isolated pieces. Alternatively, two outer isolated plates can be added for purpose of shielding, and this method is discussed below.

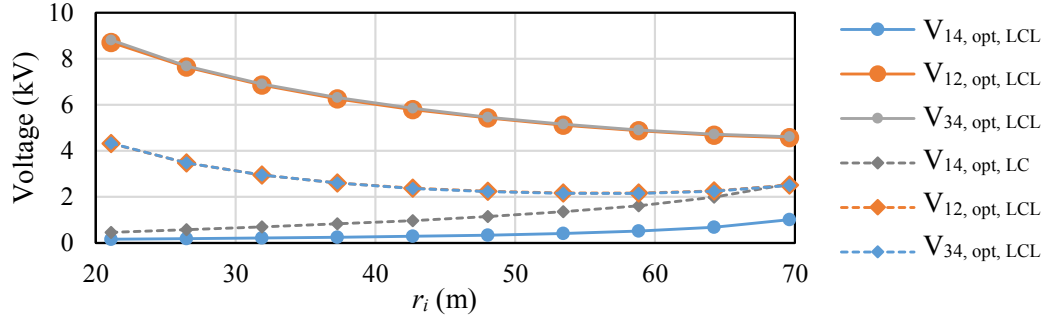


Fig. 5.5: Impact of the inner plate size on  $V_{14}$ ,  $V_{12}$ , and  $V_{34}$  for LCL and LC compensations.

## 5.2 Design with Shielding Plates

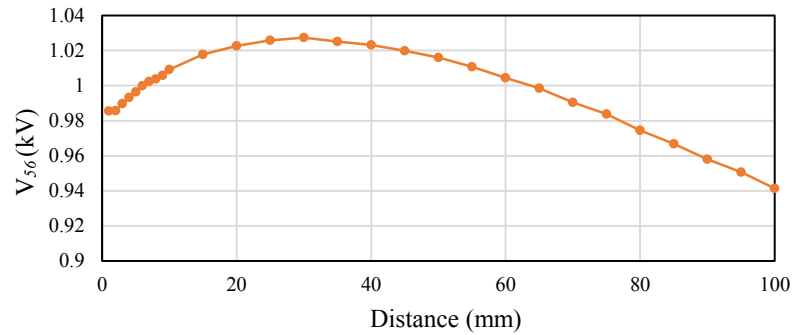


Fig. 5.6: Impact of distance of shielding plates on  $V_{56}$  for LCL compensation ( $r_{SH}=50$  cm,  $P_{out}=300$ ).



When shielding plates P5 and P6 are added, a six-plate coupler system is obtained. In six-plate structure, the active zone is determined by the voltage between shielding plates P5 and P6,  $V_{56}$ . A lateral six-plate structure is studied and analytically described in [29], but the same derivations hold for a vertical six-plate coupler:

$$V_{56} = V_1 \frac{C_{M13}}{C_3} + V_2 \frac{C_{M13}}{C_3} \quad (5.1)$$

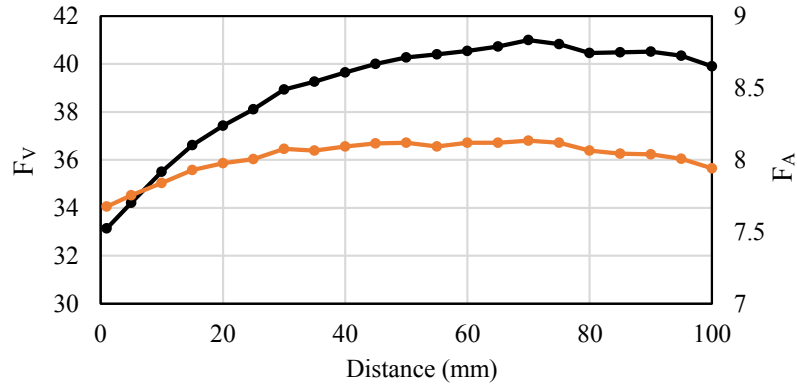


Fig. 5.7: Impact of distance of shielding plates on  $F_V$  and  $F_A$ .

where the method how to calculate  $C_{M13}$ ,  $C_{M23}$  and  $C_3$  is described in detail in [29]. From Fig.4.9, one can derive relation between  $V_1$ ,  $V_2$  and  $I_2$ :

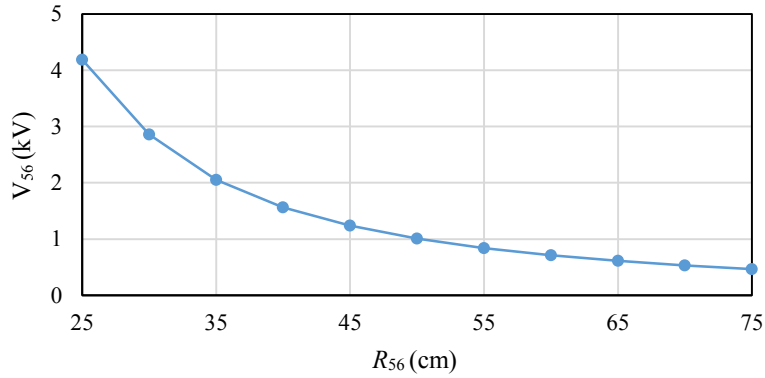


Fig. 5.8: Impact of size of shielding plates on  $V_{56}$  ( $d_{SH}=8$  mm,  $P_{out}=300$  W).

$$j\omega_s C_M \mathbf{V}_1 + \mathbf{I}_2 = j\omega_s C_2 \mathbf{V}_2 \quad (5.2)$$

Substituting  $V_1$  from (5.2) into (5.1),  $V_{56}$  can be expressed in the standard form as similar to (4.6) that is used for  $V_{14}$ :

$$\mathbf{V}_{56} = -\frac{\mathbf{I}_2}{j\omega_s C_X} + \alpha_C \mathbf{V}_2 \quad (5.3)$$

where:

$$\alpha_C = \frac{C_2 C_{M13}}{C_M C_3} + \frac{C_{M23}}{C_3} \quad C_X = \frac{C_M C_3}{C_{M13}} \quad (5.4)$$

Equation (5.4) allow the same optimization procedure to be conducted, as described in Section 4.1 for LC and in Section 4.2 for LCL compensations. In the analysis below, LCL compensation is adopted and the system is optimized for the minimum active zone. Beside the optimization of compensation elements, the design is tested regarding the optimum distance of shielding plates and the coupler and with respect an optimum radius of shielding plates. Fig.5.6 reveals that the distance between the shielding plates and the coupler have a marginal impact on voltage  $V_{56}$  and  $d_{SH}=8$  mm is adopted for further analysis. When size of the shielding plates is increases, voltage  $V_{56}$  drops. Interestingly, that does not reduce  $F_A$ , since the area of the coupler increases, neutralizing the positive impact of  $V_{56}$  reduction. Unlike  $F_A$ ,  $F_V$  reduces when for larger shielding plates.

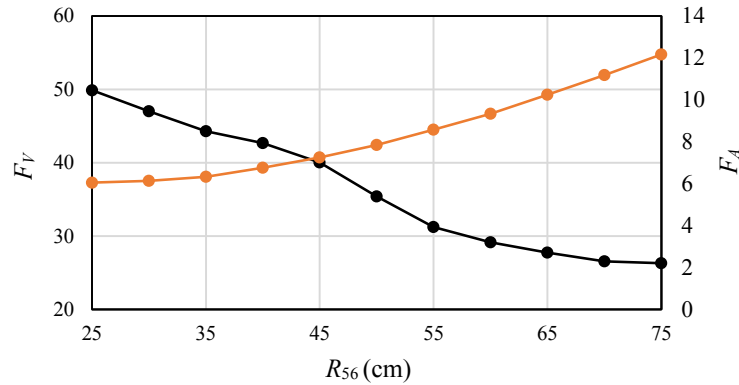


Fig. 5.9: Impact of size of shielding plates on  $F_V$  and  $F_A$ .

CHAPTER 6  
EFFICIENCY ANALYSIS OF FOUR PLATE CPT COUPLERS

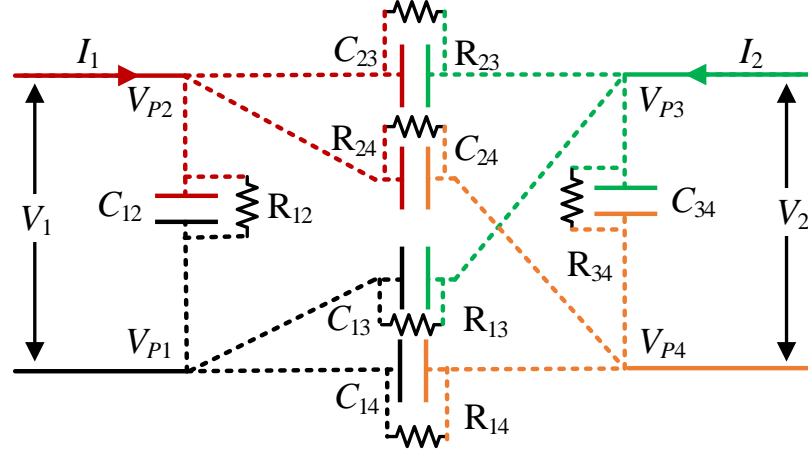


Fig. 6.1: Inclusive model of CPT coupler with losses.

In any real electric circuit there are losses. In case of V4PC, these losses are presented in the form of plate resistances. These plate resistances have been represented in Fig.6.2. The behavioral model has further been modified to include losses modelling Fig.6.1.

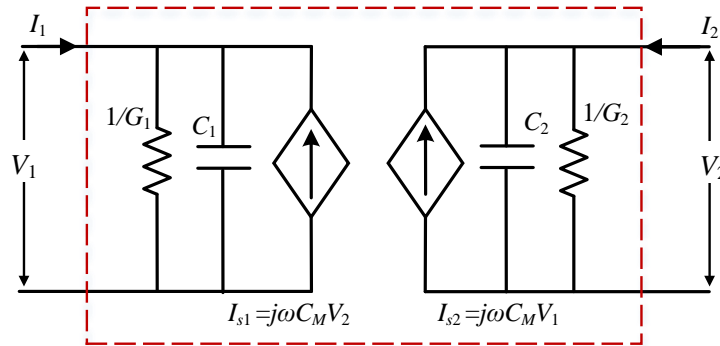


Fig. 6.2: Behavioral model with modeled eddy current losses in the plate.

The conductance's  $G_1$  and  $G_2$  can be calculated as :

$$G_1 = G_{12} + \frac{(G_{13} + G_{14})(G_{23} + G_{24})}{G_{13} + G_{14} + G_{23} + G_{24}} \quad (6.1)$$

$$G_2 = G_{34} + \frac{(G_{14} + G_{24})(G_{13} + G_{23})}{G_{13} + G_{14} + G_{23} + G_{24}} \quad (6.2)$$

### 6.1 Double-Sided LC compensation

For a LC compensation, the input admittance on the receiver side is:

$$Y_{in} = j\omega(C_2 + C_{2,ext}) + G_2 + \frac{1}{j\omega L_2 + R_L} \quad (6.3)$$

The reflected admittance on primary side is:

$$Y_{ref} = \frac{\omega^2 C_M^2}{Y_{in}} \quad (6.4)$$

$$\frac{\omega^2 C_M^2}{Y_{in}} = \frac{\omega^2 C_M^2 (j\omega L_2 + R_L)}{j\omega R_L (C_2 + C_{2,ext}) + G_2 (j\omega L_2 + R_L)} \approx \frac{\omega^2 C_M^2 (j\omega L_2 + R_L)}{j\omega R_L (C_2 + C_{2,ext}) + j\omega L_2 G_2} \quad (6.5)$$

The reflected resistance on the primary side is given by:

$$R_{ref} = \frac{R_L (C_2 + C_{2,ext})}{\omega^2 C_M^2 L_2} + \frac{G_2}{\omega^2 C_M^2} \quad (6.6)$$

Hence, the output power can be calculated as:

$$P_{out} = \frac{|V_{in}|^2}{(\omega L_1)^2} R_{ref} = \frac{|V_{in}|^2}{(\omega L_1)^2} \left( \frac{\frac{1}{G_1}}{\frac{R_L (C_2 + C_{2,ext}) + L_2 G_2}{\omega^2 C_M^2 L_2} + \frac{1}{G_1}} \right)^2 \frac{R_L (C_2 + C_{2,ext})}{\omega^2 C_M^2 L_2} \quad (6.7)$$

which can further be approximated as :

$$P_{out} = P_{out,0} P_{Lf} \quad (6.8)$$

$$P_{out,0} = |V_{out}| |V_{in}| \omega \frac{(C_1 + C_{1,ext})(C_2 + C_{2,ext})}{C_M} \quad (6.9)$$

$$P_{Lf} = \frac{1}{R_L \frac{(C_2 + C_{2,ext})^2 G_1}{C_M^2} + \frac{G_2 G_1}{\omega^2 C_M^2} + 1} \quad (6.10)$$

where,  $P_{out,0}$  represents the output power in an ideal circuit and  $P_{Lf}$  corresponds to a loss factor.

## CHAPTER 7

### EXPERIMENTAL RESULTS

#### 7.1 Experimental Setup

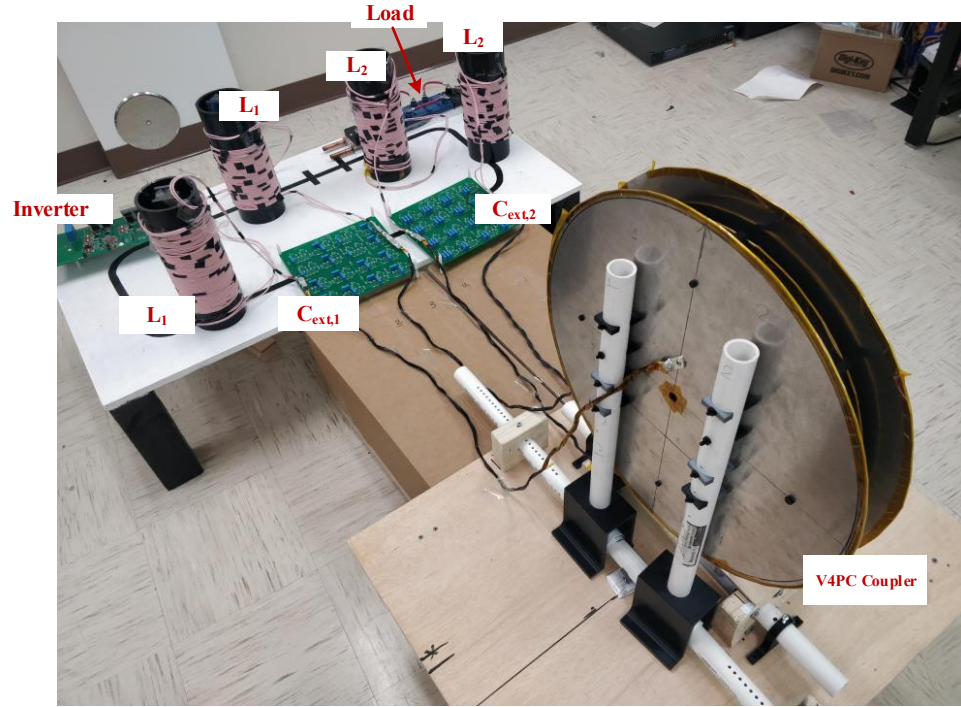


Fig. 7.1: Experimental Setup.

Table 7.1: Experimental V4PC Specifications

Parameters	Value
$r_C$	25 cm
$d_C$	61 mm
$r_i$	21.1 cm
$d_i$	12 cm

Table 7.2: LCR meter measurements for capacitance calculation

Serial No.	Terminal 1	Terminal 2	Value
1	1,2	3,4	$C_{S,1}, R_{S,1}$
2	1,4	2,3	$C_{S,2}, R_{S,2}$
3	1,3	2,4	$C_{S,3}, R_{S,3}$
4	1	2,3,4	$C_{S,4}, R_{S,4}$
5	2	1,3,4	$C_{S,5}, R_{S,5}$
6	3	1,2,4	$C_{S,6}, R_{S,6}$

A down-scaled experimental setup is built in the lab. The experiments have been scaled down to ensure that all the components and lab measurement instruments operate within their limits, e.g. that the voltage levels are within measurement limits of voltage probes. Aluminum plates and PVC pipes are utilized to build V4PC structure as shown in Fig. 7.1. The dimensions of the couplers are in the Table 7.1. The setup allows movements to create lateral and longitudinal misalignment conditions. The terminal wires are appropriately spaced to reduce the parasitic capacitance. Appropriately rated heat shrink tubes and Kapton tapes are used for effective insulation.

Table 7.3: Circuit Parameters

Parameters	Value	Parameters	Value
$V_{inv}$	45 V	$V_{out}$	38.5 V
$f_s$	500 kHz		
$C_{12}, R_{12}$	114.4 pF, 0.65 M $\Omega$	$C_{23}, R_{23}$	41.7 pF, 2.08 M $\Omega$
$C_{13}, R_{13}$	4.8 pF, 22 M $\Omega$	$C_{24}, R_{24}$	4.8 pF, 22 M $\Omega$
$C_{14}, R_{14}$	12 pF, 9.25 M $\Omega$	$C_{34}, R_{34}$	114.4 pF, 0.65 M $\Omega$
Equivalent circuit parameters			
$C_1, 1/G_1$	126.7 pF, 0.6 M $\Omega$	$C_2, 1/G_2$	126.7 pF, 0.6 M $\Omega$
$C_M$	7.54 pF		

A PCB is designed for connecting  $C_{1,ext}$  and  $C_{2,ext}$  to the circuit. This board has terminals to connect multiple capacitors in series and parallel. Series connection of capacitors allows higher voltage rating, while parallel connection allows higher current rating. This helps us in realization of multiple values of capacitances while ensuring that each individual

capacitor on the board operates within its rated value.

The circuit parameters of V4PC are measured with an LCR meter. The model parameters cannot be measured directly and the LCR meter measurements are complex combination of circuit parameters. Therefore, Multiple measurements are taken by combining the terminals of four plates and matrix operations are performed to get model parameters values. The Table 7.2 shows the combinations made for taking the measurements. Terminal 1 and Terminal 2 are the LCR meter terminals connected to the circuit terminals (1,2,3,4).

## 7.2 Optimisation Results

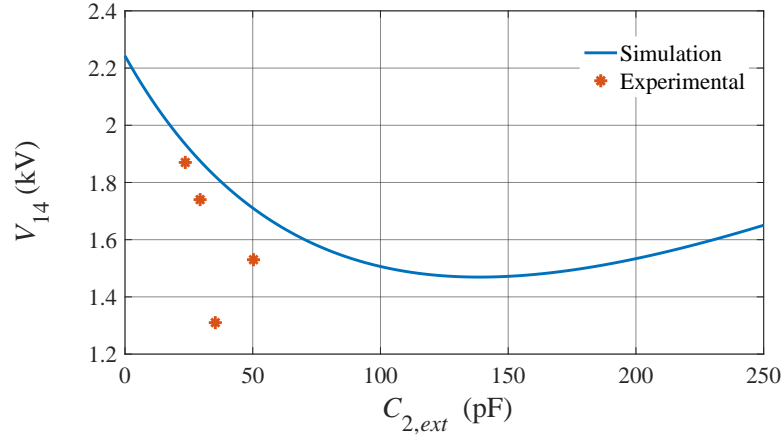


Fig. 7.2:  $V_{14}$  as a function of  $C_{2,ext}$ .

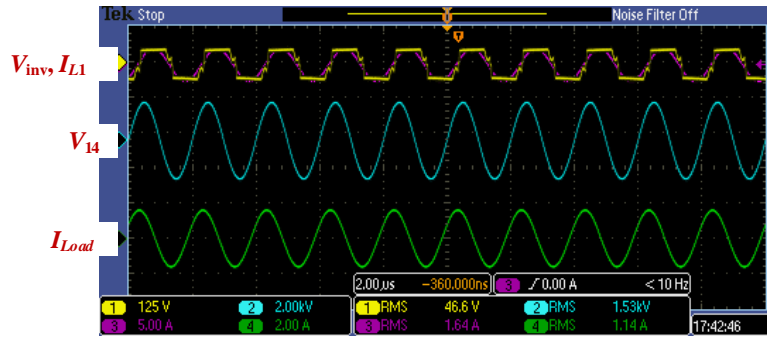


Fig. 7.3: Voltage ( $V_{inv}$ ,  $V_{14}$ ) and current ( $I_{L1}$ ,  $I_{Load}$ ) waveforms ( $C_{2,ext}=50.3$  pF)



The experimental and simulation results are plotted in Fig. 7.2 for  $V_{14}$  as a function of  $C_{2,ext}$ . The optimum  $V_{14}$  from simulation can be observed at 140 pF. Due to scarcity of time and resources, the number of experimental points were limited to four. The four experimental points are at 23.6 pF, 29.4 pF, 35.4 pF, and 50.3 pF corresponding to 1.87 kV, 1.74 kV, 1.31 kV, and 1.53 kV, respectively. However, these four points give us an approximate location of optimum  $V_{14}$ . It can be observed that the optimum  $V_{14}$  of the experimental results is shifted further left than simulation and analytical results are predicting. The waveform for  $C_{2,ext}=50.3$  pF is shown in Fig. 7.3.

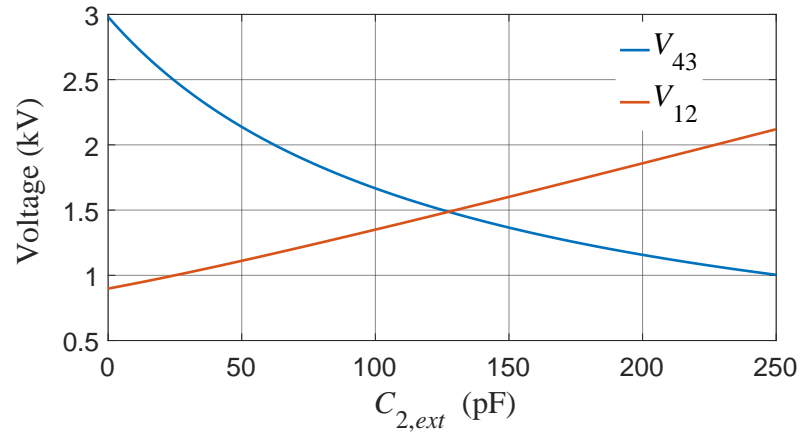


Fig. 7.4:  $V_{43}$  and  $V_{12}$  as functions of  $C_{2,ext}$ .

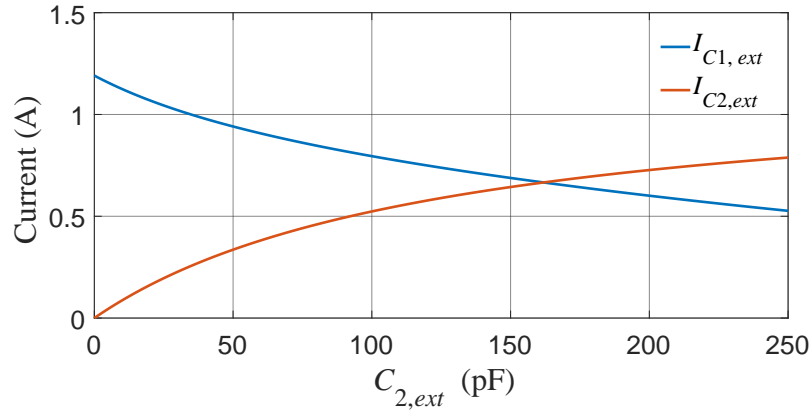


Fig. 7.5:  $I_{C1,ext}$  and  $I_{C2,ext}$  as a function of  $C_{2,ext}$ .

The simulation results for the variation of  $V_{43}$  and  $V_{12}$  as functions of  $C_{2,ext}$  are shown in Fig. 7.4. It can be observed that  $V_{43}$  decreases with increase in  $C_{2,ext}$ , while  $V_{12}$  increases as  $C_{2,ext}$  increases. It is clear that near the optimum point, the voltage rating of the components will be minimum. Since, higher voltage rating corresponds to more expensive components, this operating point is more economically viable. The same is true for current rating of capacitors  $C_{1,ext}$  and  $C_{2,ext}$ , as shown in Fig. 7.5.

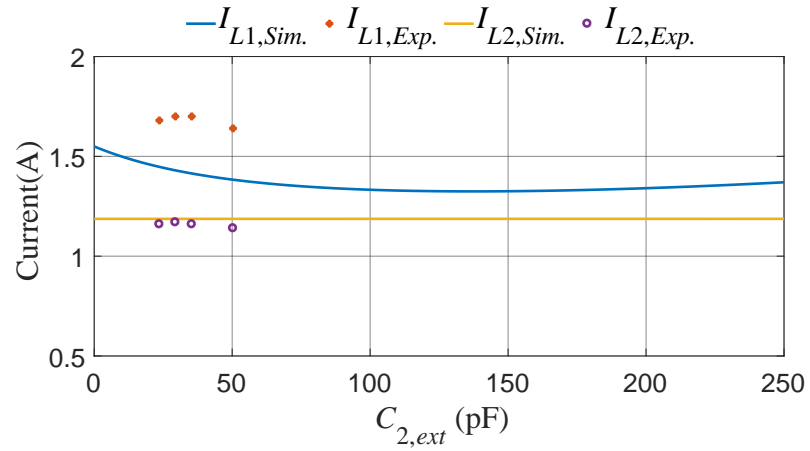


Fig. 7.6:  $I_{L1}$  and  $I_{L2}$  as a function of  $C_{2,ext}$ .

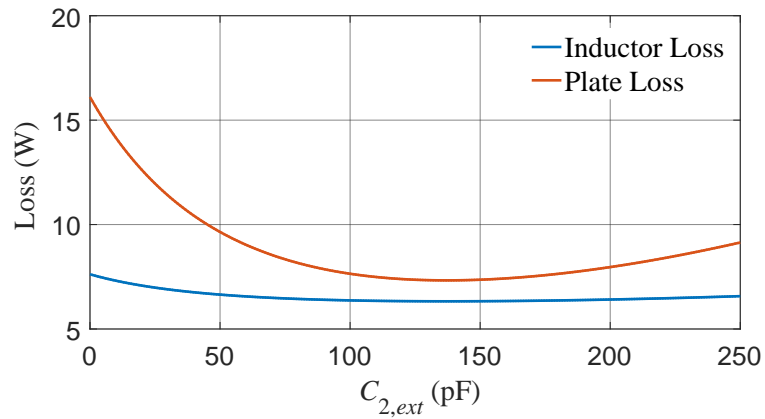


Fig. 7.7: Inductor ESR and plate losses as function of voltage  $V_{14}$ .

The variation of  $I_{L1}$  and  $I_{L2}$  as functions of  $C_{2,ext}$  is shown in fig. 7.6. It can be

observed that  $I_{L2}$  remains constant as it is load current. However,  $I_{L1}$  has a minima near the optimum point. Operating at this point will result in low losses in the inductors as losses are proportional to  $I_{L2}$ . There is difference between  $I_{L1}$  simulation and  $I_{L1}$  experimentation results. It is most likely due to the error in loss modelling and effect of input parasitics of measuring instrument on the circuit. This problem has been discussed again at the end of this chapter.

The simulation results for inductor losses and coupler plate losses as function of  $C_{2,ext}$  are shown in Fig. 7.7. It can be observed that the plate loss is minimum near optimum point. The efficiency and output power are shown in Fig. 7.8. The maximum efficiency and optimum point are not same. However, It can be observed that the efficiency is still relatively better at optimum point compared to boundary values.

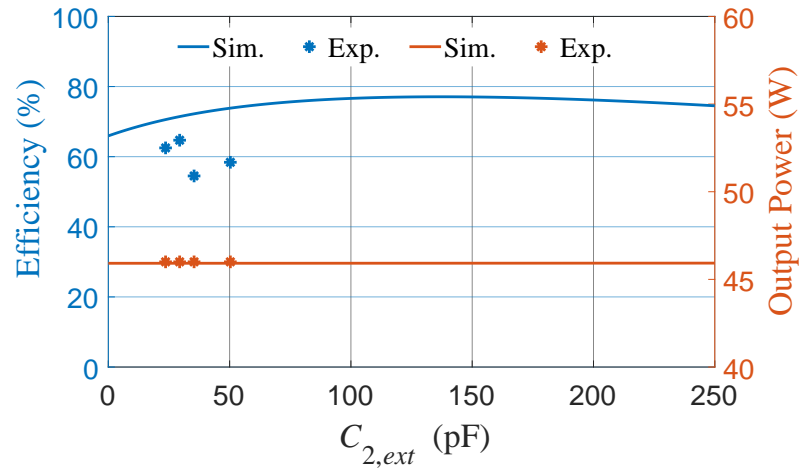


Fig. 7.8: Efficiency and output power as a function of  $C_{2,ext}$ .

There can be multiple factors which can lead to this difference in experimental and simulation results. The two key factors are:

### 7.2.1 Input Capacitance of Voltage Probe

The input capacitance of a voltage probe connected to measure  $V_{14}$  adds to the existing  $C_{14}$ , causing a parasitic non-modeled coupling between the primary and secondary. In

general, the capacitance of the voltage probe is in order pF's, which is comparable to coupler capacitance  $C_{14}$ . This parasitic effect causes the mistuning of the circuit. If the system is tuned taking into account this capacitance, then the characterization of the original system is no more valid. A probe with low input capacitance should be used to mitigate this effect.

### **7.2.2 Precision of LCR meter and Losses**

The ESR of inductors must be included for accurate modelling of the circuit. High operating frequency along with large inductance values gives rise to high quality factor ( $>1500$ ). The LCR meter gives significant error when the quality factor of inductor is above thousand.

## CHAPTER 8

### CONCLUSION

In this research, the impact of the design of LC and LCLC compensation networks on leakage electric field is studied. The results of this study is used to minimize the area around a V4PC coupler where leakage electric field is above safety limits. FEM analysis and MATLAB simulink circuit modelling are utilized to conduct this research.

A comprehensive optimization algorithm is be developed. An experimental setup is built to verify optimization results. The experiment results point out to an optimum compensation which minimizes the size of active zone. Moreover, efficiency analysis is also developed. However, there are difference between the simulation and experimental results. These differences can be reduced by increasing the operating frequency and using instruments with minimum parasitic capacitances.

## REFERENCES

- [1] G. A. Covic and J. T. Boys, “Modern trends in inductive power transfer for transportation applications,” *IEEE Journal of Emerging and Selected topics in power electronics*, vol. 1, no. 1, pp. 28–41, 2013.
- [2] R. Tavakoli and Z. Pantic, “Analysis, design, and demonstration of a 25-kw dynamic wireless charging system for roadway electric vehicles,” *IEEE Journal of Emerging and Selected Topics in Power Electronics*, vol. 6, no. 3, pp. 1378–1393, 2018.
- [3] F. Lu, H. Zhang, and C. Mi, “A review on the recent development of capacitive wireless power transfer technology,” *Energies*, vol. 10, no. 11, p. 1752, 2017.
- [4] R. Jegadeesan, K. Agarwal, Y.-X. Guo, S.-C. Yen, and N. V. Thakor, “Wireless power delivery to flexible subcutaneous implants using capacitive coupling,” *IEEE Transactions on Microwave Theory and Techniques*, vol. 65, no. 1, pp. 280–292, 2017.
- [5] S. Aldhafer, P. D. Mitcheson, J. M. Arteaga, G. Kkelis, and D. C. Yates, “Lightweight wireless power transfer for mid-air charging of drones,” in *2017 11th European Conference on Antennas and Propagation (EUCAP)*. IEEE, 2017, pp. 336–340.
- [6] T. McGinnis, C. P. Henze, and K. Conroy, “Inductive power system for autonomous underwater vehicles,” in *OCEANS 2007*. IEEE, 2007, pp. 1–5.
- [7] E. Gdoutos, C. Leclerc, F. Royer, M. D. Kelzenberg, E. C. Warmann, P. Espinet-Gonzalez, N. Vaidya, F. Bohn, B. Abiri, M. R. Hashemi *et al.*, “A lightweight tile structure integrating photovoltaic conversion and rf power transfer for space solar power applications,” in *2018 AIAA Spacecraft Structures Conference*, 2018, p. 2202.
- [8] C. C. Mi, G. Buja, S. Y. Choi, and C. T. Rim, “Modern advances in wireless power transfer systems for roadway powered electric vehicles,” *IEEE Transactions on Industrial Electronics*, vol. 63, no. 10, pp. 6533–6545, 2016.
- [9] C. T. Rim and C. Mi, *Wireless power transfer for electric vehicles and mobile devices*. John Wiley & Sons, 2017.
- [10] A. Azad, R. Tavakoli, U. Pratik, B. Varghese, C. Coopmans, and Z. Pantic, “A smart autonomous wpt system for electric wheelchair applications with free-positioning charging feature,” *IEEE Journal of Emerging and Selected Topics in Power Electronics*, 2018.
- [11] A. Yakovlev, S. Kim, and A. Poon, “Implantable biomedical devices: Wireless powering and communication,” *IEEE Communications Magazine*, vol. 50, no. 4, pp. 152–159, 2012.
- [12] S. Jung and K. B. Ariyur, “Automated wireless recharging for small uavs,” *International Journal of Aeronautical and Space Sciences*, vol. 18, no. 3, pp. 588–600, 2017.

- [13] T. Kan, Y. Zhang, Z. Yan, P. P. Mercier, and C. C. Mi, "A rotation-resilient wireless charging system for lightweight autonomous underwater vehicles," *IEEE Transactions on Vehicular Technology*, vol. 67, no. 8, pp. 6935–6942, 2018.
- [14] J. Dai, D. C. Ludois *et al.*, "A survey of wireless power transfer and a critical comparison of inductive and capacitive coupling for small gap applications," *IEEE Trans. Power Electron*, vol. 30, no. 11, pp. 6017–6029, 2015.
- [15] J. Dai and D. C. Ludois, "Capacitive power transfer through a conformal bumper for electric vehicle charging," *IEEE J. Emerg. Sel. Top. Power Electron*, vol. 4, no. 3, pp. 1015–1025, 2016.
- [16] T. M. Mostafa, A. Muharam, and R. Hattori, "Wireless battery charging system for drones via capacitive power transfer," in *Emerging Technologies: Wireless Power Transfer (WoW)*, 2017 IEEE PELS Workshop on. IEEE, 2017, pp. 1–6.
- [17] W. Zhou, Y. Su, L. Huang, X. Qing, and P. A. Hu, "Wireless power transfer across metal barrier by combined capacitive and inductive coupling," *IEEE Transactions on Industrial Electronics*, 2018.
- [18] A. Kumar, S. Pervaiz, C.-K. Chang, S. Korhummel, Z. Popovic, and K. K. Afridi, "Investigation of power transfer density enhancement in large air-gap capacitive wireless power transfer systems," in *2015 IEEE Wireless Power Transfer Conference (WPTC)*. IEEE, 2015, pp. 1–4.
- [19] H. Zhang, F. Lu, H. Hofmann, W. Liu, and C. C. Mi, "A four-plate compact capacitive coupler design and lcl-compensated topology for capacitive power transfer in electric vehicle charging application," *IEEE Transactions on Power Electronics*, vol. 31, no. 12, pp. 8541–8551, 2016.
- [20] F. Lu, H. Zhang, H. Hofmann, and C. C. Mi, "A double-sided lc-compensation circuit for loosely coupled capacitive power transfer," *IEEE Transactions on Power Electronics*, vol. 33, no. 2, pp. 1633–1643, 2018.
- [21] F. Lu, H. Zhang, H. Hofmann, and C. Mi, "A double-sided lclc-compensated capacitive power transfer system for electric vehicle charging," *IEEE Transactions on Power Electronics*, vol. 30, no. 11, pp. 6011–6014, 2015.
- [22] L. J. Zou, A. P. Hu, and Y.-g. Su, "A single-wire capacitive power transfer system with large coupling alignment tolerance," in *2017 IEEE PELS Workshop on Emerging Technologies: Wireless Power Transfer (WoW)*. IEEE, 2017, pp. 93–98.
- [23] B. Ge, D. C. Ludois, and R. Perez, "The use of dielectric coatings in capacitive power transfer systems," in *2014 IEEE Energy Conversion Congress and Exposition (ECCE)*. IEEE, 2014, pp. 2193–2199.
- [24] T. Komaru and H. Akita, "Positional characteristics of capacitive power transfer as a resonance coupling system," in *Wireless Power Transfer (WPT)*, 2013 IEEE. IEEE, 2013, pp. 218–221.

- [25] S. Li, Z. Liu, H. Zhao, L. Zhu, C. Shuai, and Z. Chen, "Wireless power transfer by electric field resonance and its application in dynamic charging," *IEEE Transactions on Industrial Electronics*, vol. 63, no. 10, pp. 6602–6612, 2016.
- [26] I. C. on Non-Ionizing Radiation Protection *et al.*, "Icnirp statement on the guidelines for limiting exposure to time-varying electric, magnetic, and electromagnetic fields (up to 300 ghz)," *Health Physics*, vol. 97, no. 3, pp. 257–258, 2009.
- [27] "Ieee standard for safety levels with respect to human exposure to radio frequency electromagnetic fields, 3 khz to 300 ghz," *IEEE Std C95.1-2005 (Revision of IEEE Std C95.1-1991)*, pp. 1–238, April 2006.
- [28] I. Ramos, K. Afridi, J. A. Estrada, and Z. Popović, "Near-field capacitive wireless power transfer array with external field cancellation," in *Wireless Power Transfer Conference (WPTC), 2016 IEEE*. IEEE, 2016, pp. 1–4.
- [29] H. Zhang, F. Lu, H. Hofmann, W. Liu, and C. C. Mi, "Six-plate capacitive coupler to reduce electric field emission in large air-gap capacitive power transfer," *IEEE Transactions on Power Electronics*, vol. 33, no. 1, pp. 665–675, 2018.
- [30] R. Love, "The electrostatic field of two equal circular co-axial conducting disks," *The Quarterly Journal of Mechanics and Applied Mathematics*, vol. 2, no. 4, pp. 428–451, 1949.
- [31] D. F. Bartlett and T. R. Corle, "The circular parallel plate capacitor: a numerical solution for the potential," *Journal of Physics A: Mathematical and General*, vol. 18, no. 9, p. 1337, 1985.
- [32] L. Fox and E. Goodwin, "The numerical solution of non-singular linear integral equations," *Philosophical Transactions of the Royal Society of London. Series A, Mathematical and Physical Sciences*, vol. 245, no. 902, pp. 501–534, 1953.